CM² MAGAZINE

第 69 期

南方科技大学海洋磁学中心主编

https://cm².sustech.edu.cn/

创刊词

海洋是生命的摇篮，是文明的纽带。地球上最早的生命诞生于海洋，海洋里的生命最终进化成了人类，人类的文化融合又通过海洋得以实现。人因海而兴。

人类对海洋的探索从未停止。从远古时代美丽的神话传说，到麦哲伦的全球航行，再到现代对大洋的科学钻探计划，海洋逐渐从人类敬畏崇拜幻想的精神寄托演变成可以开发利用与科学研究的客观存在。其中，上个世纪与太空探索同步发展的大洋科学钻探计划将人类对海洋的认知推向了崭新的纬度：深海（deep sea）与深时（deep time）。大洋钻探计划让人类知道，奔流不息的大海之下，埋藏的却是亿万年的地球历史。它们记录了地球板块的运动，从而使板块构造学说得到证实；它们记录了地球环境的演变，从而让古海洋学方兴未艾。

在探索海洋的悠久历史中，从大航海时代的导航，到大洋钻探计划中不可或缺的磁性地层学，磁学发挥了不可替代的作用。这不是偶然，因为从微观到宏观，磁性是最基本的物理属性之一，可以说，万物皆有磁性。基于课题组的学科背景和对海洋的理解，我们对海洋的探索以磁学为主要手段，海洋磁学中心因此而生。

海洋磁学中心，简称 CM^2，一为其全名“Centre for Marine Magnetism”的缩写，另者恰与爱因斯坦著名的质能方程 $E = MC^2$ 对称，借以表达我们对科学巨匠的敬仰和对科学的不懈追求。

然而科学从来不是单打独斗的产物。我们以磁学为研究海洋的主攻利器，但绝不仅限于磁学。凡与磁学相关的领域均是我们关注的重点。为了跟踪反映国内外地球科学特别是与磁学有关的地球科学领域的最新研究进展，海洋磁学中心特地主办 CM^2 Magazine，以期与各位地球科学工作者相互交流学习、合作共进！

“海洋孕育了生命，联通了世界，促进了发展”。 21 世纪是海洋科学的时代，由陆向海，让我们携手迈进中国海洋科学的黄金时代。

目 录

一、研究进展

1. 海洋磁异常记录的过去 11 Ma 地球磁场古强度的连续变化

地磁场是地球的保护伞，阻止了太阳风和宇宙高能粒子袭击地球。因此，地磁场的强度和方向变化规律及机制，一直是最前沿的科学问题。之前，人们对地磁场强度变化的认识主要依赖沉积物记录。长时间尺度的记录需要非常厚的沉积序列，受此限制，目前科学家只构建出了 8 百万以来的强度变化特征。沉积物记录有复杂性和多解性，我们急需独立的记录来验证这些特征，同时，我们需要进一步拓延地磁场强度变化时序。

除了沉积物，从大洋中脊下喷出大量玄武岩形成洋壳。这些洋壳也是能记录地磁场信息的良好介质。基于新的算法与严格的数据检验，南方科技大学海洋科学与工程系海洋磁学（CM^2）团队通过对洋壳上观测到的海洋磁异常数据的处理和分析，构建出目前最长的（11 百万年以来）连续的球磁场强度变化曲线。

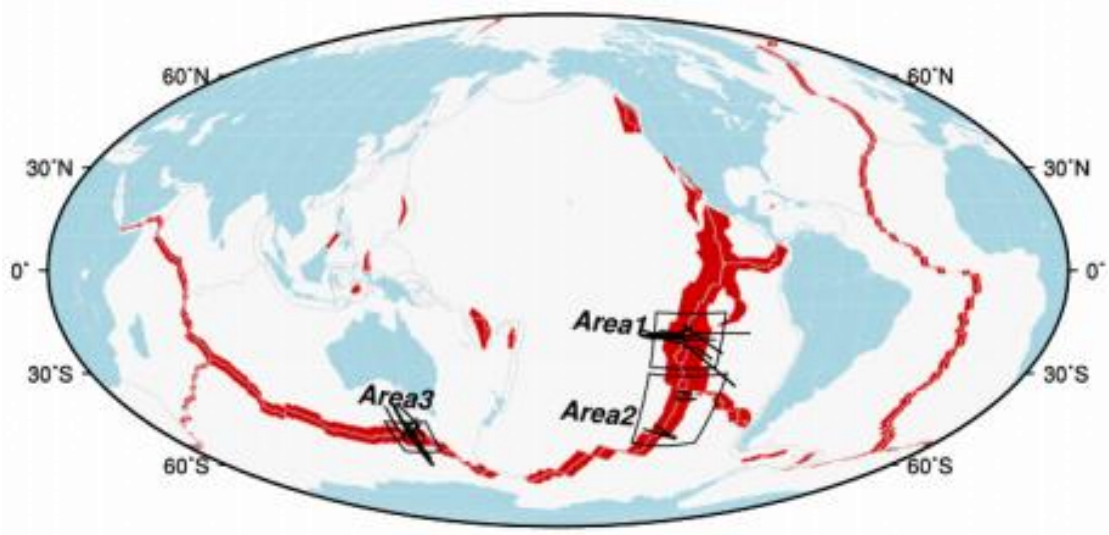

图 1 三个研究区域的位置图。图中红色阴影表示 0-11 Ma 的洋壳分布，黑线表示每个区域挑选出来的磁异常剖面。

研究区域位于太平洋和印度洋三个快速扩张洋脊 (图 1)。首先对磁异常剖面进行误差分析，提高信噪比；然后通过信号分析处理，去掉地表地形和纬度不均一等的影响；接着确定剖面上倒转边界的位置和年龄框架；最后通过不同区域的数据叠加，削弱了局部磁异常的影响，最终获得了不同区域的三条综合磁异常曲线 (图 2)。

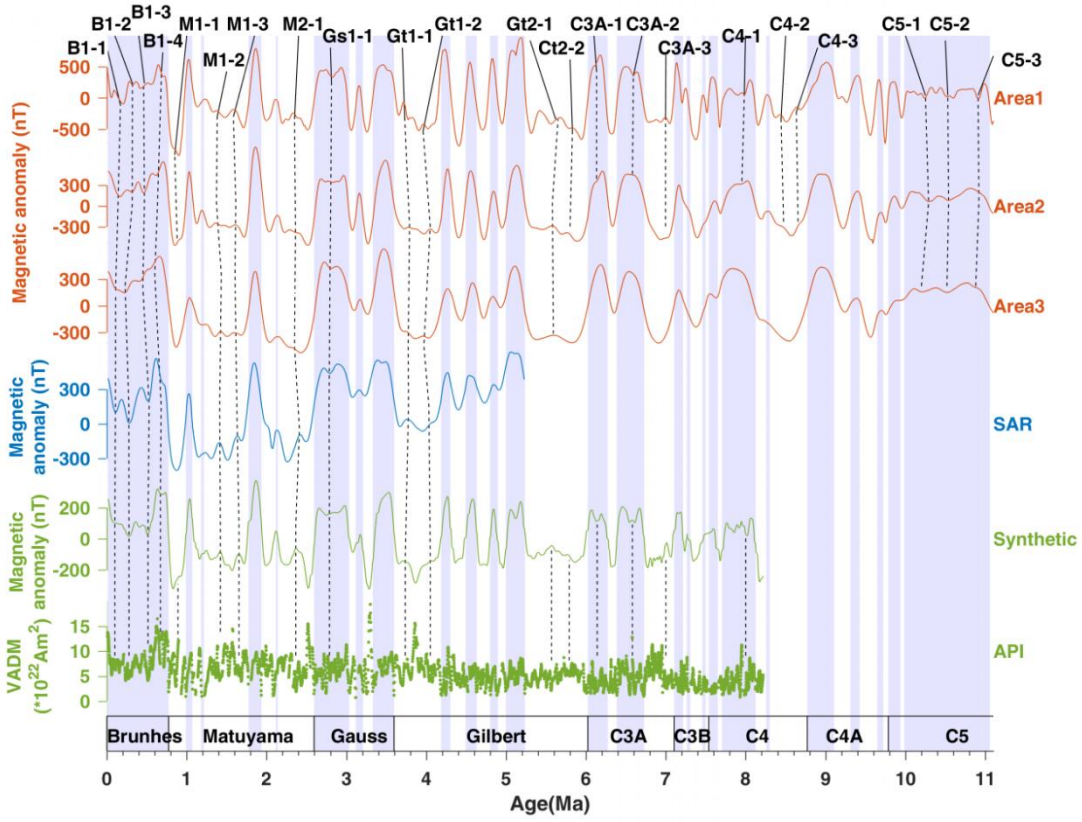

图 2 三条磁异常叠加剖面(红色)，南大西洋的磁异常记录(蓝色)和沉积物得到相对强度转换成绝对强度(绿点)以及模拟磁异常曲线(绿线)的比较。

研究结果显示，地磁场强度除了具有大尺度变化特征外，还额外叠加了很多20-40 万年的短波长异常，标记为 B、M、G、C 系列。通过将这三条磁异常剖面与其它方法获得的数据进行比较，发现不同方法得出的短波长变化规律非常一致(图 2)，验证这些特征的可靠性，证实这些短波长异常反映的是地球磁场古强度的波动。

CM^2 团队构建的 11 百万年以来地磁场强度的波动特征，反映出地磁场的长时序不稳定性，为地磁场变化提供了重要依据。此外，这些特征还可为长时间尺度沉积物记录提供年代学参考。

该成果发表于 Geophysical Research Letters. *Li, Y., Liu, J., & Liu, Q. (2021).* ***Geomagnetic Field Paleointensity Spanning the Past 11 Myr from Marine Magnetic Anomalies in the Southern Hemisphere.*** *Geophysical Research Letters, 48, e2021GL093235. https://doi.org/10.1029/2021GL093235.* 以上研究得到了国家自然科学基金（41704068, 41874078 和 U1606401）、国家重点研发计划（2016YFA061903）与深圳市科创委（KQTD20170810111725321）的支持。

作者：李园洁，南方科技大学海洋科学与工程系，主要研究方向：海洋古地磁、海洋磁异常。

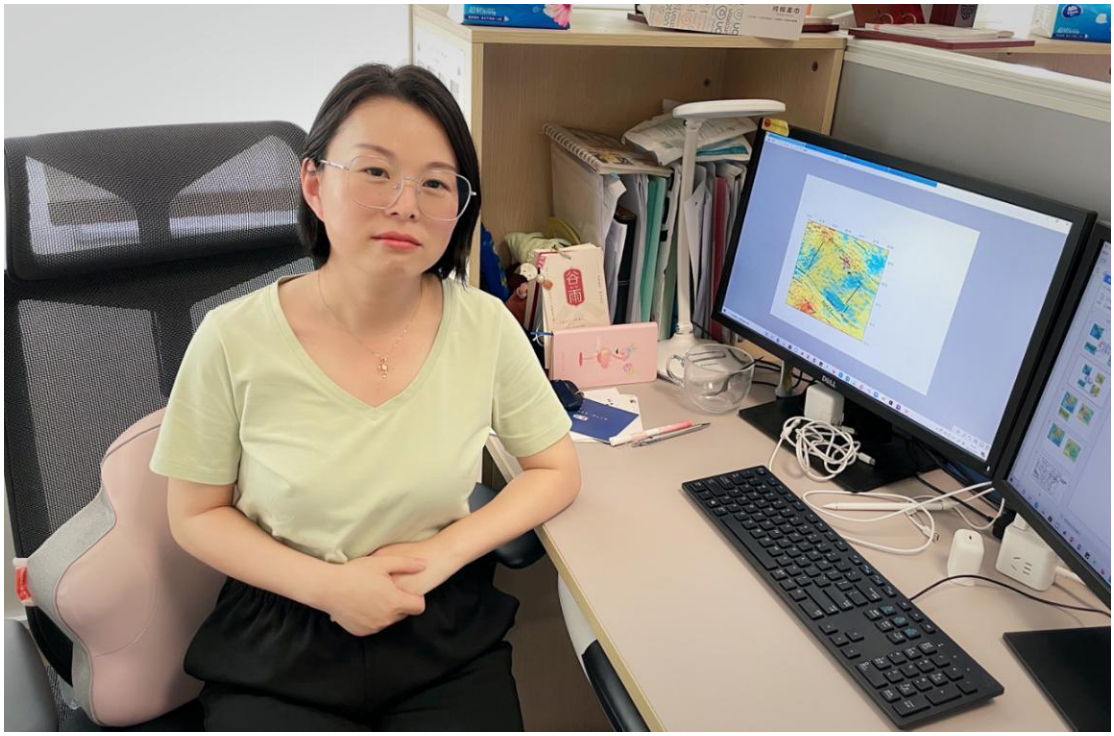

二、文献进展

1. 千年尺度反馈机制决定了冰川终止时期的形态和速度

翻译人：仲义 zhongy@sustech.edu.cn

Barker S, Knorr G. ***Millennial scale feedbacks determine the shape and rapidity of glacial termination*** *[J]. Nature Communications, 2021, 12(1): 2273.*

https://doi.org/10.1038/s41467-021-22388-6

总结和展望：在晚更新世时期，冰川终止时期描绘了在冰期旋回结束时的转换变化特征。虽然海洋/大气系统的突变是冰消期主要组成部分，但是它们的具体作用过程及其终止时期受大振幅的快速震荡事件影响仍然存在很多不确定性。本文观点认为这些冰期终止时期不确定性主要是由于千年尺度和轨道时间尺度交互作用的产物。具体来说，作者讨论了这种反馈机制的重要性，这些反馈似乎主要出现在千年尺度活动的最为突出的时期，特别是在冰川终止时期，这有助于解释这些事件发生的规模和速度。然后，作者提出了 AMOC 稳定性结构的变化可以解释终止时期发生 AMOC 震荡事件，如 HS1-B/A-YD 事件。最后，作者认为在 Termination 1 时期 AMOC 异常震荡导致全新世 CO_2 的较低初始浓度和快速上升，而其本身就被认为是不寻常的（不需要人类的干预）。

然而，在我们认识中仍然有很大的空白需要更多假设和实验来进行验证。例如，在最后一次冰河时期之后海平面重建是不确定和不一致的（尤其在 MIS 3、MIS 5a/4、Termination 2），这使得在检验 AMOC 稳定性变化是否为海洋环流冰消期震荡变化的驱动因素以及在评估冰期-间冰期时间尺度上千年尺度变化的边界控制方面存在困难。因此，我们需要更有说服力的海平面重建，才能使得我们能够比较二氧化碳上升和冰盖下降的相对速度，并对作者关于 B/A-YD 震荡的独特性进行判断。

过去几年中，许多重要的理论发现都是通过单一模型获得的，这使得他们的结果容易受到特定模型可能存在的缺陷的影响。PMIP 计划等项目使人们对于各

种不同模型设置中非强制如没有淡水控制的 AMOC 震荡进行比较也更有信心。迄今为止，大多数对气候突变的模拟都是通过用淡水强迫进行模拟，但越来越多的结果显示“非强制”震荡（或是对逐渐变化的边界条件的强非线性响应）。考虑到淡水强迫以外的因素明显重要性，作者提倡通过其他方式模拟突变气候。最终，通过碳循环和冰盖动态过程相互作用（包括固体地球和冰架裂解过程）的结合，可以为地球耦合系统中涉及机制带来更充分的描述。通过这种方式，我们将能够极大地提高对气候内部系统动力学如何应对外部作用力的理解，并最终在我们对冰川终止时期变化理解上达到一个转折点。这种知识不仅仅是学术上的重要问题，关于当前气候稳定性阈值位置的不确定性意味着我们不能排除这样一种可能性，即相对于北大西洋淡水强迫作用，AMOC 变化可能已经处于多重均衡的体制之内。

Summary and outlook: In this perspective we have highlighted progress in our understanding of glacial terminations as the ultimate expression of the interaction between millennial and orbital-timescale variations in Earth’s climate. Specifically we discussed the importance of feedbacks, which appear most accentuated within the sweet spot of millennial activity, and in particular during glacial termination when they help to explain the magnitude and rapidity of these events. We then made the case that structural changes in the stability of the AMOC can explain the occurrence of terminal AMOC oscillations such as the HS1-B/A-YD triptych. Finally we argued that the unusual AMOC oscillation of Termination 1 led to the low initial concentration and subsequent rise of atmospheric CO_2 throughout the Holocene, which itself may therefore be considered unusual a priori (without the need to call on human intervention).

However, there are still major gaps in our knowledge, which need to be filled before we can test some of the hypotheses put forward here. For example, sea-level reconstructions beyond the last glacial maximum are uncertain and inconsistent (e.g. throughout MIS 3 and across MIS 5a/4 and Termination 2; Fig. 4), making it difficult to test our ideas about changing AMOC stability as a driver for deglacial oscillations in ocean circulation or even to assess the boundary controls on the occurrence of

millennial-timescale variability on G-IG timescales. More robust sea-level reconstructions are therefore required that will allow us to compare the relative rates of CO_2 rise and ice sheet decline during previous terminations and assess our assertions for example about the uniqueness of the B/A-YD oscillation.

An area of gathering momentum is model intercomparison. Many of the exciting theoretical discoveries made over the past few years have been obtained using a single model, leaving their results vulnerable to possible inadequacies in a particular model. Projects such as PMIP94,95 will allow more confidence to be gained (or not) in proposed mechanisms as will efforts to compare unforced (e.g. without freshwater forcing) AMOC oscillations in a variety of different model setups. To date most simulations of abrupt climate variability have been forced with freshwater but a growing number of models display forms of 'unforced' oscillations (or at least strongly non-linear responses to gradually changing boundary conditions). Given the apparent importance of factors other than freshwater forcing we advocate a community effort to simulate abrupt transitions through other means. Ultimately, the incorporation of an interactive carbon cycle and ice sheet dynamics (including e.g. solid earth and ice shelf cavity processes) will allow a fuller representation of the mechanisms involved in the coupled earth system. In this way we will be able to vastly improve our understanding of how internal climate system dynamics respond to external forcing across deglacial transitions and finally reach a turning point in our understanding of glacial terminations. This knowledge is not merely of academic interest; uncertainties over the location of stability thresholds with respect to our current climate mean that we cannot rule out the possibility that the AMOC is already within a regime of multiple equilibria with respect to North Atlantic freshwater forcing.

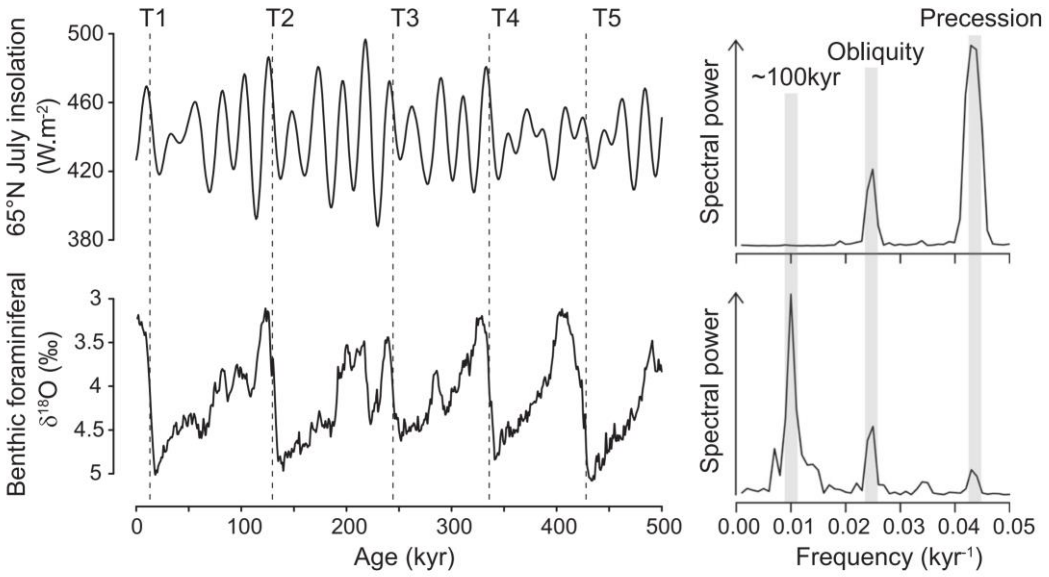

Figure 1. The 100 kyr problem. The geologic record of benthic foraminiferal $\delta^{18}O$ contains significant spectral power in the eccentricity band (as well as those of precession and obliquity) while the external insolation forcing at this period (~100 kyr) is negligible. Late Pleistocene glacial cycles are 'terminated' by relatively short deglacial periods, giving rise to a characteristic saw-tooth character. T1–T5 represent Terminations 1 to 5.

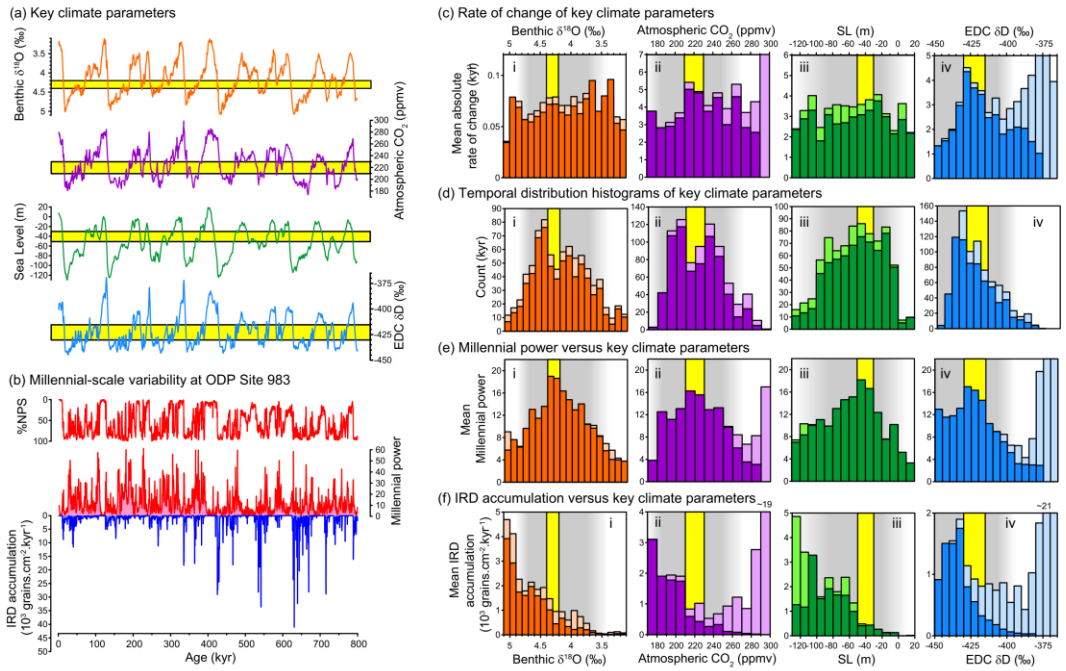

Figure 2. The sweet spot of millennial variability. a Records of benthic $\delta^{18}O$, atmospheric CO_2, sea level and Antarctic δD. Yellow bars are same as for c–f. b Records from ODP Site 98325: %NPS (a

proxy for sea surface temperature), millennial power (Hilbert transform of the 0.5–7 kyr Taner bandpass filtered %NPS record) and Ice Rafted Debris (IRD) accumulation. c Binned mean absolute rates of change for the records in a. d Distribution histograms of the records in a. e Mean millennial power for the same bins utilized in c, d. f Mean IRD accumulation rates for the same bins utilized in c, d. In each panel fainter colours represent deglacial intervals (terminations) while bolder colours represent all other times. Yellow bars highlight the respective peaks in millennial power in e (the sweet spot as described in the text and Box 1) and grey shaded regions highlight the broader windows of opportunity.

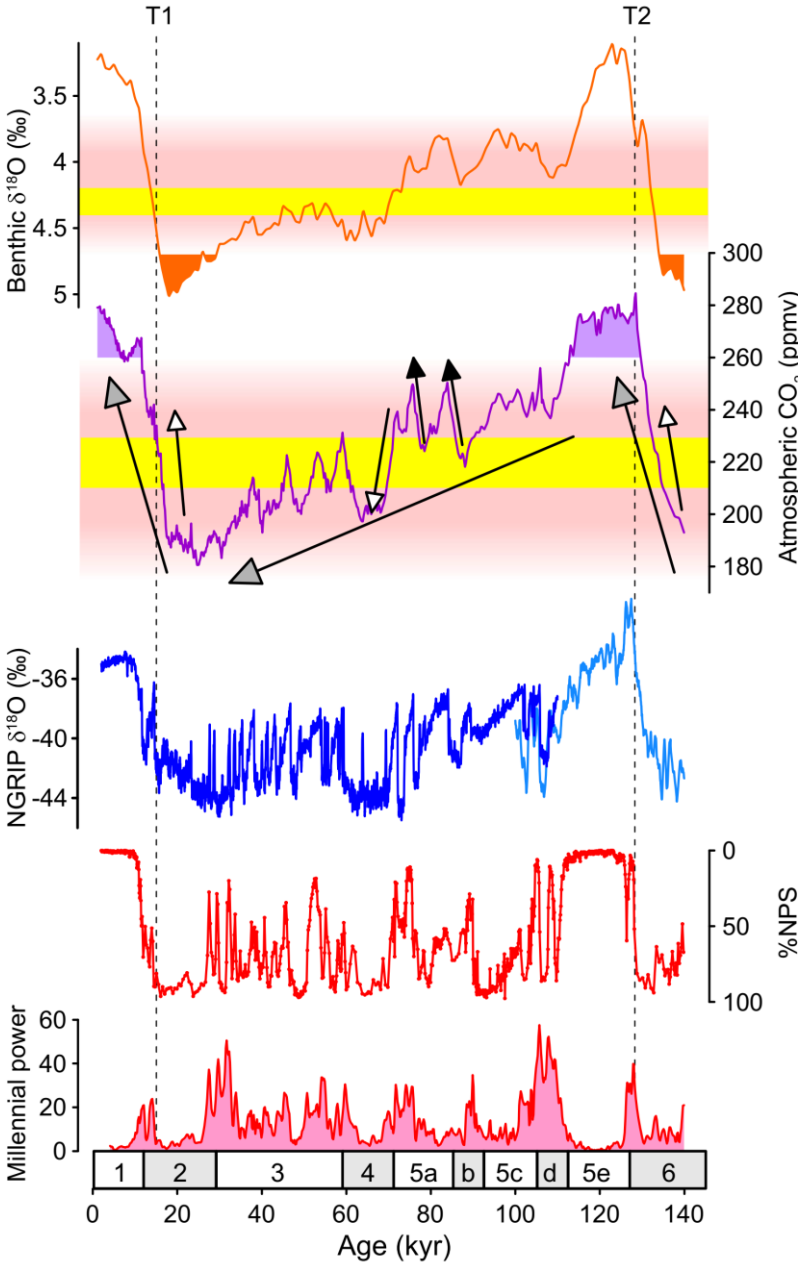

Figure 3. Feedbacks between millennial and orbital-timescale variability. From top to bottom: Benthic $\delta^{18}O$ (filled regions indicate monostable AMOC as a function of maximum ice volume); Atmospheric CO_2 (filled regions indicate monostable AMOC as a function of high CO_2); Greenland ice-core $\delta^{18}O$ with synthetic record beyond 110ka; %NPS (temperature proxy) from ODP Site 983; Millennial activity at Site 983 (see text). Pink and yellow shaded boxes represent the window of opportunity and sweet spot respectively (see Fig. 2). Grey headed arrows represent orbitaltimescale trends in atmospheric CO_2; Black (white) headed arrows represent examples of negative (positive) feedback of millennial-scale variability on orbital changes. Feedbacks are strongest within the sweet spot. Dashed vertical lines indicate timing of AMOC recovery associated with glacial terminations T1 and T2. Lower numbers are Marine Isotope Stages.

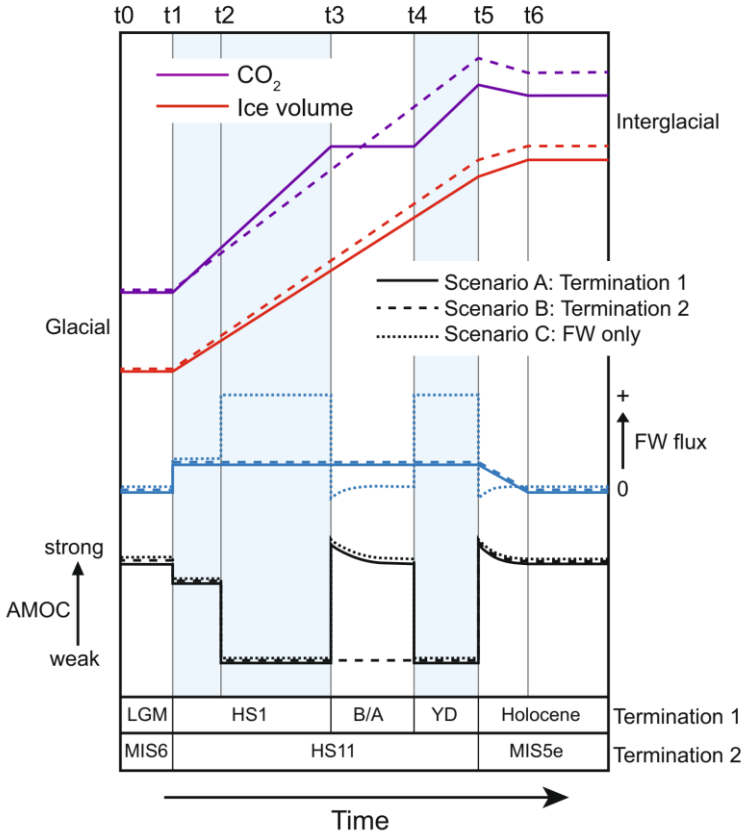

Figure 4. Deglacial changes in structural stability. Idealised timeseries of CO_2, ice volume and North Atlantic freshwater (FW) flux for last two terminations with corresponding variations in AMOC strength according to text and Fig. 4. Solid curves represent T1; Dashed curves represent T2; Dotted curves represent a scenario for T1 in which variations in the AMOC are forced purely by freshwater (not requiring an underlying structural change in stability). Times t0–t6 are referred to in text.

2. 北美东部 Acadian 造山带的深部岩浆堆晶根

翻译人：冯婉仪 fengwy@sustech.edu.cn

Tassara S, Ague J J, Valencia V. ***The deep magmatic cumulate roots of the Acadian orogen, eastern North America*** *[J]. Geology, 2021, 49: 168-173.*

https://doi.org/10.1130/G47887.1

摘要：增生造山带中堆晶岩浆根的缺乏是地壳内质量和能量重新分配导致中-酸性岩浆岩形成这一模型的基础。同样，由于缺乏相关的同时代深部镁铁质岩石，在美国东北部新英格兰阿巴拉契亚山脉中演化的泥盆纪 Acadian 岩浆作用的起源长期以来被认为是封闭系统的地壳熔融作用导致的。在这里，我们发现了 Acadian 含水超镁铁质堆晶岩，它们是由来自地幔的母岩熔体（美国新英格兰南部康涅狄格州）的在深部（~ 1.1 GPa）经历分离结晶过程而形成的。这些岩石是在阿巴拉契亚造山带发现的第一批此类岩石，也是世界上为数不多的保存下来的弧下深部含水堆晶岩。我们提出所研究的岩石与新英格兰中南部同时代的演化的深成岩之间存在成因联系，其中前者代表同一岩浆弧中缺失的深部堆晶根。研究结果支持了幔源含水岩浆在地壳深部的分离结晶和同化混染作用是导致中-酸性岩浆产生和大陆地壳地球化学演化的基本过程这一假说。

ABSTRACT: The dearth of cumulate magmatic roots in accretionary orogens is a cornerstone of models that postulate redistribution of mass and energy within the crust for the genesis of intermediate to silicic magmatism. Likewise, the origin of the evolved Acadian (Devonian) plutonism in the New England Appalachians (northeastern USA) has long been explained by closed-system crustal melting due to the absence of associated coeval deep mafic counterparts. Here, we report the discovery of Acadian hydrous ultramafic cumulate rocks that formed by deepseated (~ 1.1 GPa) fractional crystallization processes from a mantle-derived parental melt (Connecticut, southern New England, USA). These rocks are the first of their kind identified in the Appalachian orogen, and one of only a handful of preserved deep subarc hydrous cumulates

worldwide. We propose a genetic link between the studied rocks and the evolved coeval plutonism in central-southern New England, where the former represent the missing deep cumulate roots of the same magmatic arc. Our findings support the hypothesis that differentiation of mantle-derived hydrous magmas by fractional crystallization and assimilation processes in the deep crust is a fundamental process in the production of intermediate to silicic magmatism and the geochemical evolution of the continental crust.

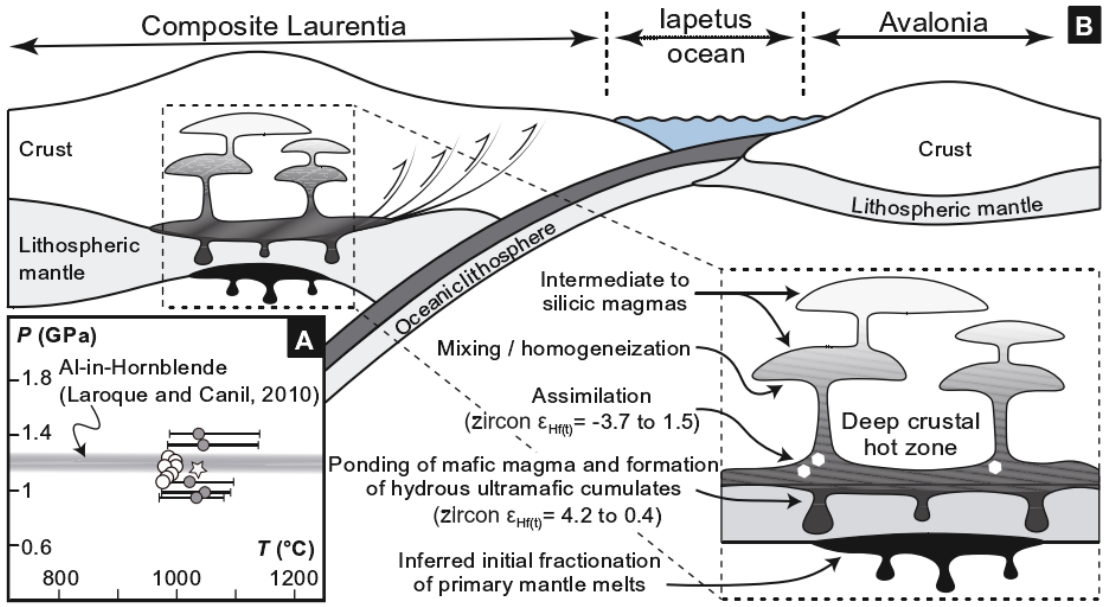

Figure 1. (A) Two-pyroxene (gray circles) and amphibole (white circles) thermobarometry. Star indicates mean two-pyroxene pressuretemperature (P-T) value. (B) Simplified geological model of tectonic and petrogenetic processes for genesis of evolved Acadian plutonism in central-southern New England, USA.

3. 过去 35 百万年海水稳定 Sr 同位素揭示的全球碳循环的波动

翻译人:李园洁 liyj3@sustech.edu.cn

Paytan A, Griffith E M, Eisenhauer A, et al. ***A 35-million-year record of seawater stable Sr isotopes reveals a fluctuating global carbon cycle*** *[J]. Science, 2021, 371(6536): 1346-1350. https://doi.org/10.1126/science.aaz9266*

摘要: 海水中主要成分的含量和同位素组成的变化可反映它们的来源和沉降的改变。由于控制着这些来源和沉降的过程大多数与碳循环有关，这样的记录可以为驱动过去大气二氧化碳和气候的机制问题提供思路。本文，作者展示了来自大洋重晶石的稳定锶（Sr）同位素记录。$\delta^{88/86}$Sr 的记录显示出复杂的模式，在过去 35-15 Ma 之间首先下降，然后在 15-5 Ma 之间增加，直到再次下降到现在。数值模拟的结果揭示出海水中 Sr 含量相对现代海水的相关波动大约±25%。作者认为 $\delta^{88/86}$Sr 数据反映了生物碳酸盐的矿物和埋藏位置的变化。

ABSTRACT: Changes in the concentration and isotopic composition of the major constituents in seawater reflect changes in their sources and sinks. Because many of the processes controlling these sources and sinks are tied to the cycling of carbon, such records can provide insights into what drives past changes in atmospheric carbon dioxide and climate. Here, we present a stable strontium (Sr) isotope record derived from pelagic marine barite. Our $\delta^{88/86}$Sr record exhibits a complex pattern, first declining between 35 and 15 million years ago (Ma), then increasing from 15 to 5 Ma, before declining again from ~5 Ma to the present. Numerical modeling reveals that the associated fluctuations in seawater Sr concentrations are about ±25% relative to present-day seawater. We interpret the $\delta^{88/86}$Sr data as reflecting changes in the mineralogy and burial location of biogenic carbonates.

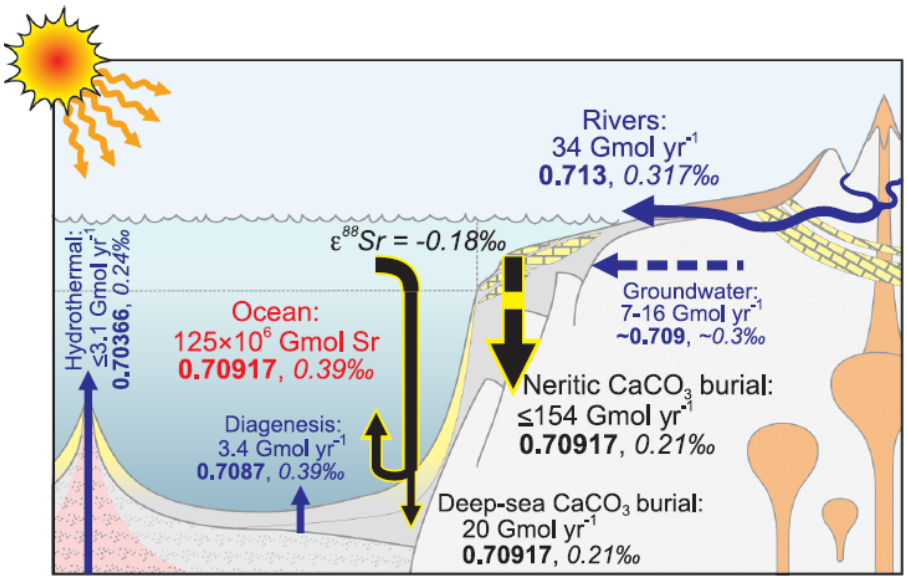

Figure 1. Schematic diagram of the modern global Sr cycle illustrating the main controlling fluxes (Gmol Sr yr^{-1}) and ocean inventory. Mean isotope values are shown in bold for radiogenic Sr and in italics for stable Sr. The present-day average flux weighted river input to the ocean has an $^{87}Sr/^{86}Sr$ of 0.713 and $\delta^{88/86}Sr$ of 0.317‰ (7), and this $\delta^{88/86}Sr$ value corresponds to an average of different lithologies (silicate 0.58‰ and carbonates 0.18‰). Groundwater inputs have an average $^{87}Sr/^{86}Sr$ ratio of 0.709 and $\delta^{88/86}Sr$ of ~0.3‰, and oceanic hydrothermal sources have an average $^{87}Sr/^{86}Sr$ ratio of 0.70366 and $\delta^{88/86}Sr$ of 0.24‰ (7). The major oceanic Sr sink is the removal of Sr into marine $CaCO_3$, which preferentially incorporates the lighter Sr isotopes with an average isotope offset e($\delta^{88/86}Sr$) of –0.18‰, resulting in average $CaCO_3$ $\delta^{88/86}Sr$ of ~0.21‰ at present (6). Seawater $^{87}Sr/^{86}Sr$ at present is 0.70917 and the $\delta^{88/86}Sr$ of seawater is 0.39‰, the latter being elevated above the $d^{88/86}Sr$ of the inputs caused by preferential removal of light Sr isotopes into $CaCO_3$ (i.e., negative e) driving seawater isotopically heavier. Dashed lines indicate more uncertain fluxes and isotopic compositions. Fluxes are compiled from the literature (see the supplementary materials). Note that available data suggest a large present-day Sr imbalance, so the Sr sink is substantially larger than the combined sources.

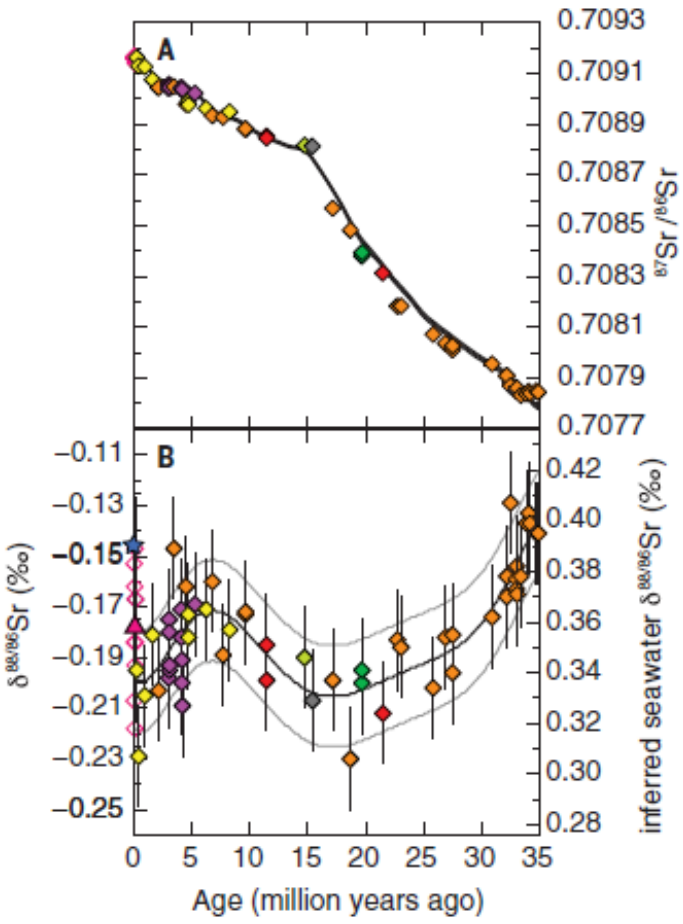

Figure 2. Sr isotope records over the past 35 Myr. (A) Radiogenic Sr isotope record in marine barite separated from several sites over the past 35 Myr (errors are smaller than the symbol size), along with the seawater Sr isotope curve (gray line) from McArthur et al. (13). Slight differences between the curves are likely due to differences in the age models used. (B) Stable Sr isotope record of these down-core marine barite samples with a polynomial curve fit (black line) ± 0.02‰ analytical uncertainty (gray lines). All data are provided in table S1. The inferred seawater $\delta^{88/86}Sr$ was determined by adding the constant isotopic offset (fractionation) of 0.536‰ based on core-top data. Site 572 is shown in yellow; Site 573, red; Site 574, orange; Site 575, green; Site 849, purple; Site 1218, dark green; and Site 1219, gray. The average δ88/86Sr core top value (–0.146‰) is marked with a blue star, and the average PC72 value (–0.178‰) is marked with a pink triangle (individual measurements are shown as open pink diamonds because they were not used in the fit); the core-top average is not included in the polynomial fit (see discussion section in the supplementary materials).

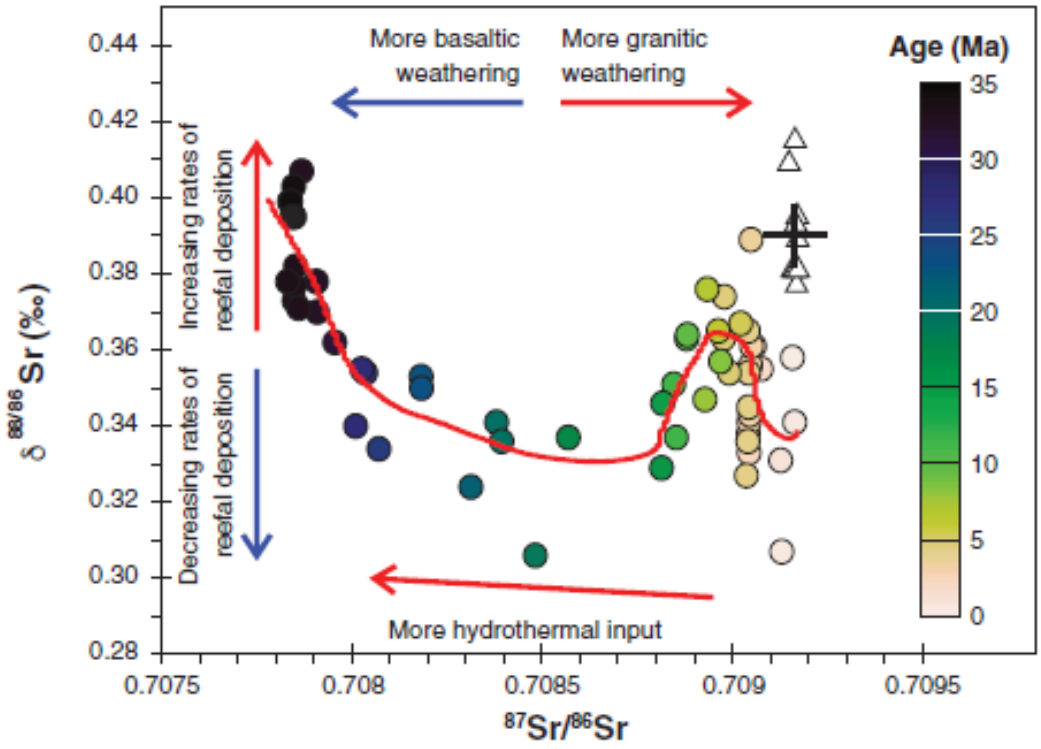

Figure 3. Observed evolution of the Sr system in radiogenic versus stable Sr isotope space over the past 35 Myr. Circles reflect down-core barite measurements and are color-coded by sample age, and triangles reflect the core-top measurements. The cross indicates modern seawater Sr isotopic composition. All barite data are corrected for the isotopic fractionation offset of 0.536‰, and the x- and y-axis scales reflect inferred seawater Sr isotopic composition rather than measured $^{87}Sr/^{86}Sr$ and $\delta^{88/86}Sr$ of barite. The red line represents the polynomial fit to the data presented in Fig. 2. The colored arrows illustrate the approximate direction in $^{87}Sr/^{86}Sr$ and $\delta^{88/86}Sr$ space of the seawater Sr response to some of the key controlling factors: the proportion of basaltic versus granitic weathering, the hydrothermal Sr input flux to the ocean, and rates of reef $CaCO_3$ deposition.

4. 华北克拉通东部侏罗纪构造演化：对古太平洋板块初始俯冲的响应

翻译人：周洋 zhouy3@sustech.edu.cn

Hao W X, Zhu R X, Zhu G. ***Jurassic tectonics of the eastern North China Craton: Response to initial subduction of the Paleo-Pacifc Plate*** *[J]. Geological Society of America Bulletin, 2021, 133: 19–36.*

https://doi.org/10.1130/B35585.1

摘要：华北克拉通（NCC）东北部的燕山褶皱冲断带（YFTB）包含一系列侏罗纪火山沉积，记录了古太平洋在 NCC 初始的俯冲。我们揭露了燕山褶皱冲断带内四个盆地的地层剖面和新的锆石 U-Pb 数据，用来约束侏罗纪地层单元的年龄和与初始俯冲有关的构造事件。经历 200-190 Ma 隆升之后，玄武岩在 188-167 Ma 持续喷发，揭示了 YFTB 最早的构造活动。玄武岩喷发形成于弧后伸展的环境中，并向西迁移，这与古太平洋板块北西西向的俯冲一致。实测数据和年代学资料表明，侏罗纪 YFTB 挤压短缩的最早阶段（燕山运动）发生在 167 Ma。这次挤压构造事件终止了侏罗纪早期至中期的岩浆作用和伸展作用，并导致了局部逆冲，隆起，形成不整合面，此次却没有剧烈的褶皱或角度不整合面的形成，是一次弱到中等强度的变形。YFTB 中的侏罗纪岩石记录了古太平洋板块俯冲初期弧后伸展。YFTB 和整个中国东部大陆的侏罗纪构造表明，古太平洋板块的初始俯冲始于约 190 Ma，并且与被动大陆边缘塌陷模型一致。

ABSTRACT: The Yanshan fold-and-thrust belt (YFTB) on the northern margin of the eastern North China Craton (NCC) contains a succession of Jurassic volcano-sedimentary rocks that record the response of the NCC to the initial stages of subduction of the Paleo-Pacifc Plate. We present stratigraphic profles and new zircon U-Pb data from four basins in the YFTB to constrain the ages of the Jurassic lithological units and tectonic events related to the initial subduction. Following uplift at 200–190 Ma, protracted eruption of basalt at 188–167 Ma reflects the earliest tectonic activity in the YFTB. The eruption occurred in a backarc extensional setting, and migrated toward the

west, consistent with WNW directed subduction of the Paleo-Pacifc Plate. The measured profiles and geochronological data demonstrate that the earliest phase of shortening in the YFTB during the Jurassic (event A of the Yanshan Movement in the Chinese literature) took place at 167 Ma. This compression terminated the magmatism and extension of the Early–Middle Jurassic, and resulted in the development of local thrusts, regional uplift, and a disconformity, without involvement of intense folding or the development of an angular unconformity. These observations are consistent with a weak to moderate intensity of deformation. The Jurassic rocks in the YFTB record the response of a backarc to the initial stages of subduction of the Paleo-Pacifc Plate. Jurassic tectonics in the YFTB and the entire eastern China continent suggests that initial subduction of the Paleo-Pacifc Plate began at ca. 190 Ma, and is consistent with the passive margin collapse model.

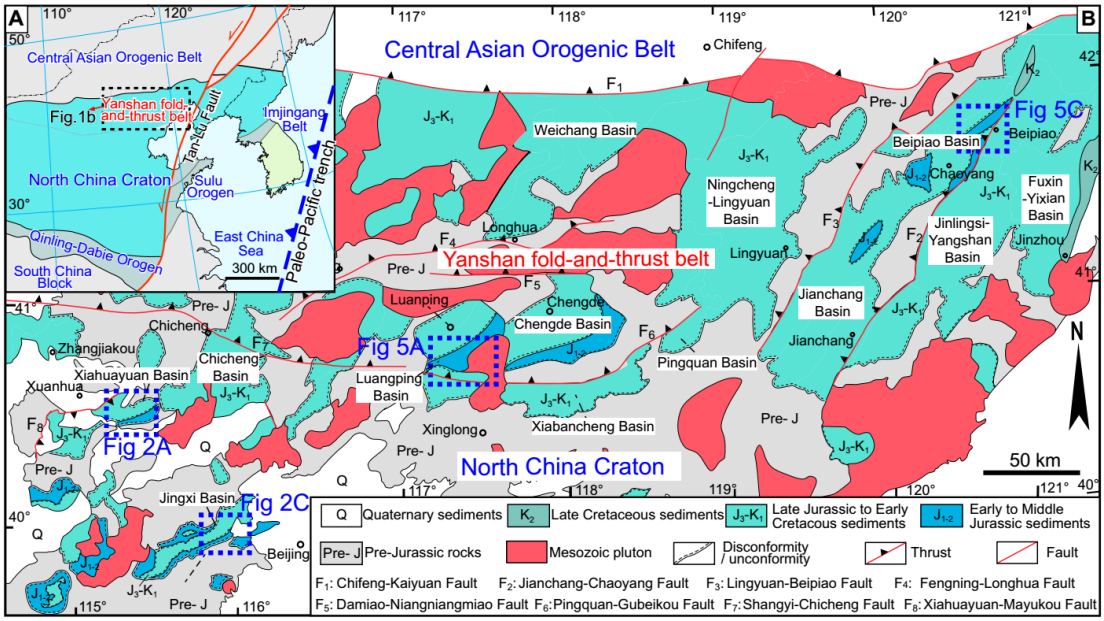

Figure 1. (A) Tectonic map of East China. (B) Sketch map showing the location of Mesozoic basins within the Yanshan fold-and-thrust belt along the northern margin of the North China Craton.

5. 中新世南极无冰区的水文影响与深海温度的联系

翻译人：张琪 zhangq7@sustech.edu.cn

Bradshaw C, Langebroek P, Lear C, et al., ***Hydrological impact of Middle Miocene Antarctic ice-free areas coupled to deep ocean temperatures*** *[J]. Nature Geoscience, 2021. https://doi.org/10.1038/s41561-021-00745-w*

摘要：用于重建过去大陆冰量的海洋沉积物氧同位素（$\delta^{18}O$）也记录了深水温度（DWTs）。传统上，这些被认为是耦合相关的（冰量变化导致 DWTs 变化）。然而，中新世暖期峰值时期（约 1600-1500 万年前）的 $\delta^{18}O$ 记录了较大的且快速的变化（约 1-1.5‰），难以用南极冰盖（AIS）体积的巨大变化来解释。利用气候模型和数据比较，我们展示了 DWTs 与 AIS 在空间范围上耦合相关，而不是体积上，因为南极的反照率变化改变了水文循环，影响了南极的深水生产区。我们认为中新世的 AIS 已经从先前的渐新世最大值大范围的后退。残余冰层在轨道时间尺度上的空间变化比以前认为的更快，使得 DWT 的波动很大（最高可达 4℃）。当中新世温暖期结束时（约 1300 万年前），大陆规模的 AIS 已经稳定，进一步的冰量变化主要是在高度上而非范围上的扩张，对 DWT 影响很小。研究结果表明，当 AIS 退缩暴露出以前被冰覆盖的土地时，海洋对冰层变化的敏感性会发生变化；相关的反馈会降低地球系统维持大型 AIS 的能力。这表明冰层变化不仅包括冰量的变化，也包括空间范围的变化。

ABSTRACT: Oxygen isotopes from ocean sediments ($\delta^{18}O$) used to reconstruct past continental ice volumes additionally record deep water temperatures (DWTs). Traditionally, these are assumed to be coupled (ice-volume changes cause DWT changes). However, $\delta^{18}O$ records during peak Middle Miocene warmth (~16–15 million years ago) document large rapid fluctuations (~1–1.5‰) difficult to explain as huge Antarctic ice sheet (AIS) volume changes. Here, using climate modelling and data comparisons, we show DWTs are coupled to AIS spatial extent, not volume, because Antarctic albedo changes modify the hydrological cycle, affecting Antarctic deep water

production regions. We suggest the Middle Miocene AIS had retreated substantially from previous Oligocene maxima. The residual ice sheet varied spatially more rapidly on orbital timescales than previously thought, enabling large DWT swings (up to 4 °C). When Middle Miocene warmth terminated (~13 million years ago) and a continent-scale AIS had stabilized, further ice-volume changes were predominantly in height rather than extent, with little impact on DWT. Our findings imply a shift in ocean sensitivity to ice-sheet changes occurs when AIS retreat exposes previously ice-covered land; associated feedbacks could reduce the Earth system's ability to maintain a large AIS. This demonstrates ice-sheet changes should be characterized not only by ice volume but also by spatial extent.

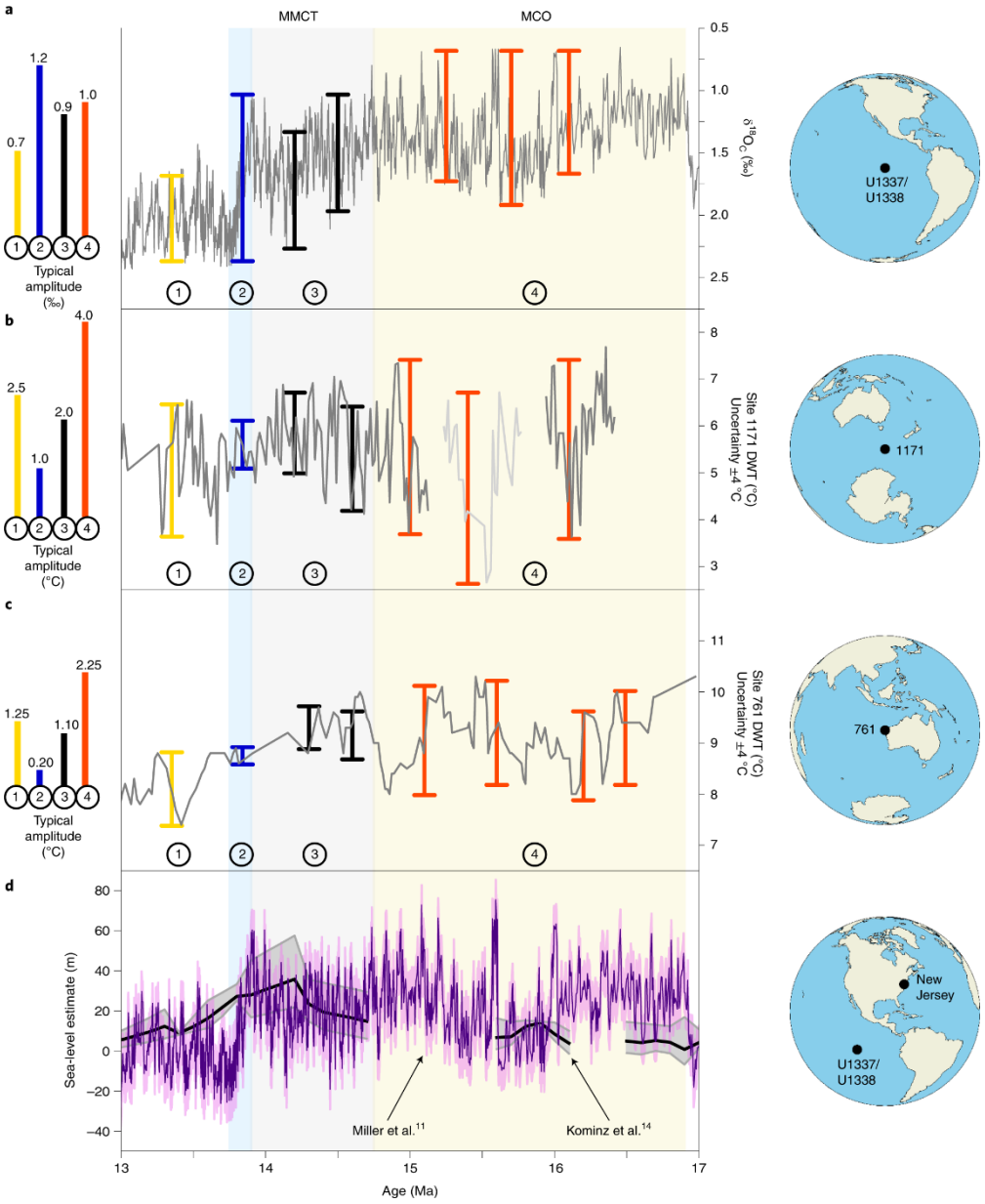

Figure 1. Middle Miocene benthic (Cibicidoides spp.) oxygen isotope, DWT and sea-level changes. a, $\delta^{18}O_c$ splice. b, Site 1171 DWT, Southern Ocean (Antarctica-proximal). c, Site 761 DWT, Indian Ocean (Antarctica-distal but in AABW path). Data locations shown on right of panels. DWTs are Mg/Ca reconstructions (uncertainty ±4 °C; relative values are considered more robust than absolutes). Other available DWT records are too low resolution/short. Data are plotted on their respective age models (full details in Supplementary Table 11). d, Sea level (eustatic estimates×1.48 cf. ref.). Shading: MCO, yellow; MMCT, blue and grey; major ice-growth event (MMCT, blue). Vertical lines are indicative of the typical maximum $\delta^{18}O_c$/DWT amplitudes during the MCO (4), MMCT before the major ice-growth event (3), MMCT major ice-growth event (2) and post-MMCT (1). Since the data cover different times and resolutions, these lines are not coincident in time for panels a–c.

6. 用于千米级无人机磁测的高速轻量标量磁力仪：传感器选择、系统设计以及输出数据质量

翻译人：曹伟 11930854@qq.com

Dssing A, Silva E, Martelet G, et al. ***A High-Speed, Light-Weight Scalar Magnetometer Bird for km Scale UAV Magnetic Surveying: On Sensor Choice, Bird Design, and Quality of Output Data*** *[J]. Remote Sensing, 2021, 13(4): 649.*

https://doi.org/10.3390/rs13040649

摘要：磁测是一种应用广泛、经济高效的遥感方法，可以应用于各种尺度下结构的探测。传统磁测以地面测量和航空测量进行，地面测量成本较低，航空测量可以获取大范围覆盖的数据。然而，地面测量通常缓慢并且获取数据不完整，而航空测量由于传感器到磁源体距离增加而不灵活、昂贵，并且会降低信噪比。随着可靠、经济的测量级无人机（UAV）的兴起和轻型磁强计的发展，一个良好设计的无人机磁测系统可以克服传统磁测系统的缺点。本文介绍了一种轻型标量场无人机集成磁强计 bird 系统（CMAGTRES-S100）的研制与测试。CMAGTRES-S100 的设计理念是形成一个高速灵活的系统，该系统无需汽车即可在野外轻松运输，可以在大多数地形和天气条件下部署，并以操作高效的方式提供高质量的标量数据，其测量范围可与次区域尺度直升机载磁测量相媲美。我们讨论了研发过程中的各个步骤，包括（i）根据传感器规格和稳定性测试选择传感器，（ii）bird 系统的设计考虑，（iii）操作效率和灵活性，以及（iv）输出数据质量。目前的 CMAGTRES-S100 系统重约 5.9 千克（包括无人机），最佳测量速度为 50 公里/小时。该系统在法国布列塔尼一个复杂的海岸环境中进行了测试，目标是镁铁质岩脉和带有磁铁矿填充物和磁铁矿块（矽卡岩）的断层接触。2.0×0.3 km 的区域由四个次区域调查结果绘制，测线间距为 10m（由于监管限制）。次区域调查在 3.5 小时内完成，包括超过 2 小时的地面机务和该区域的安全净空。研究获得了 ±0.02nT 噪声级，并绘制了若干关键地质构造图。

ABSTRACT: Magnetic surveying is a widely used and cost-efficient remote sensing method for the detection of subsurface structures at all scales. Traditionally, magnetic surveying has been conducted as ground or airborne surveys, which are cheap and provide large-scale consistent data coverage, respectively. However, ground surveys are often incomplete and slow, whereas airborne surveys suffer from being inflexible, expensive and characterized by a reduced signal-to-noise ratio, due to increased sensor-to-source distance. With the rise of reliable and affordable survey-grade Unmanned Aerial Vehicles (UAVs), and the developments of light-weight magnetometers, the shortcomings of traditional magnetic surveying systems may be bypassed by a carefully designed UAV-borne magnetometer system. Here, we present a study on the development and testing of a light-weight scalar field UAV-integrated magnetometer bird system (the CMAGTRES-S100). The idea behind the CMAGTRES-S100 is the need for a high-speed and flexible system that is easily transported in the field without a car, deployable in most terrain and weather conditions, and provides high-quality scalar data in an operationally efficient manner and at ranges comparable to sub-regional scale helicopter-borne magnetic surveys. We discuss various steps in the development, including (i) choice of sensor based on sensor specifications and sensor stability tests, (ii) design considerations of the bird, (iii) operational efficiency and flexibility and (iv) output data quality. The current CMAGTRES-S100 system weighs ~5.9 kg (including the UAV) and has an optimal surveying speed of 50 km/h. The system was tested along a complex coastal setting in Brittany, France, targeting mafic dykes and fault contacts with magnetite infill and magnetite nuggets (skarns). A 2.0×0.3 km area was mapped with a 10 m line-spacing by four sub-surveys (due to regulatory restrictions). The sub-surveys were completed in 3.5 h, including >2 h for remobilisation and the safety clearance of the area. A noise-level of ±0.02 nT was obtained and several of the key geological structures were mapped by the system.

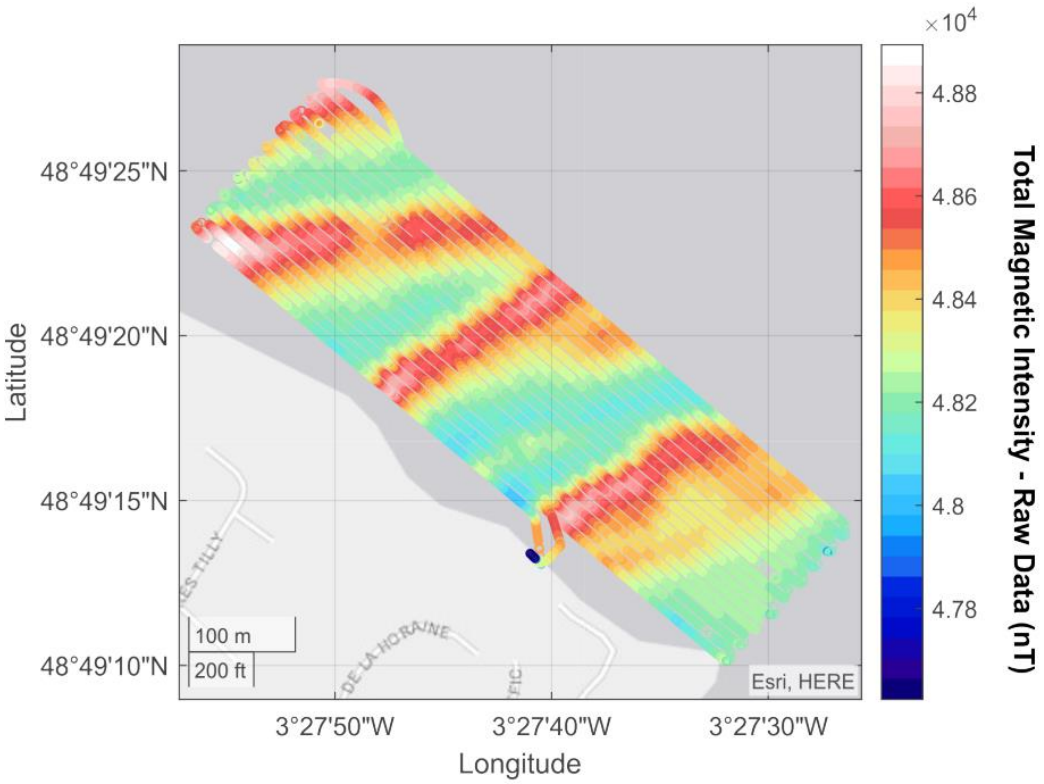

Figure 1. Fourth order difference noise estimate of the trimmed survey data, down sampled to 40 Hz.

7. 新生代海平面和冰盖演化：来自深海地球化学和大陆边缘的记录

翻译人：王敦繁 dunfan_w@foxmail.com

Miller K G, Browning J V, Schmelz W J, et al. ***Cenozoic sea-level and cryospheric evolution from deep-sea geochemical and continental margin records*** *[J]. Science Advances, 2020, 6(20): eaaz1346.*

https://doi.org/10.1126/sciadv.aaz1346

摘要：应用太平洋底栖有孔虫的$\delta^{18}O$我们估算得到了一个新生代（66 Ma）全球平均海平面（GMSL）变化范围，重建了从始新世早期无冰到第四纪两极冰层的演化。这些 GMSL 估算值与大陆边缘的“背斜”估算值具有统计相似性，这些估算值包括压实、荷载和热沉降。在峰值温度、GMSL 升高、高 CO_2 和无冰“温室”条件（56 至 48 Ma）之后，出现“冷温室”（48 至 34 Ma）冰期（10 至 30 m 变化）。大陆尺度冰盖（“冰屋”）开始时间约为 34Ma（海平面变化>50m）、南极东部盛行冰盖的时间约为 12.8Ma，两极冰川作用出现时间约为 2.5 Ma。GMSL 大幅下降（27 至 20 ka~130 m）之后，又在 19 至 10 ka 出现缓慢回升（40 mm/ yr），之后又出现减速回升（10 至 2 ka），以及静止状态，直到 1900 CE，回升速率开始增加。长尺度 CO_2 含量增加导致温暖气候和海平面升高，周期性的 Milankovitch 旋回为海平面升降的主要控制因素。

ABSTRACT: Using Pacific benthic foraminiferal $\delta^{18}O$ and Mg/Ca records, we derive a Cenozoic (66 Ma) global mean sea level (GMSL) estimate that records evolution from an ice-free Early Eocene to Quaternary bipolar ice sheets. These GMSL estimates are statistically similar to “backstripped” estimates from continental margins accounting for compaction, loading, and thermal subsidence. Peak warmth, elevated GMSL, high CO_2, and ice-free “Hothouse” conditions (56 to 48 Ma) were followed by “Cool Greenhouse” (48 to 34 Ma) ice sheets (10 to 30 m changes). Continental-scale ice sheets (“Icehouse”) began ~34 Ma (>50 m changes), permanent East Antarctic ice sheets at 12.8 Ma, and bipolar glaciation at 2.5 Ma. The largest GMSL fall (27 to 20 ka; ~130

m) was followed by a >40 mm/yr rise (19 to 10 ka), a slowing (10 to 2 ka), and a stillstand until ~1900 CE, when rates began to rise. High long-term CO_2 caused warm climates and high sea levels, with sea-level variability dominated by periodic Milankovitch cycles.

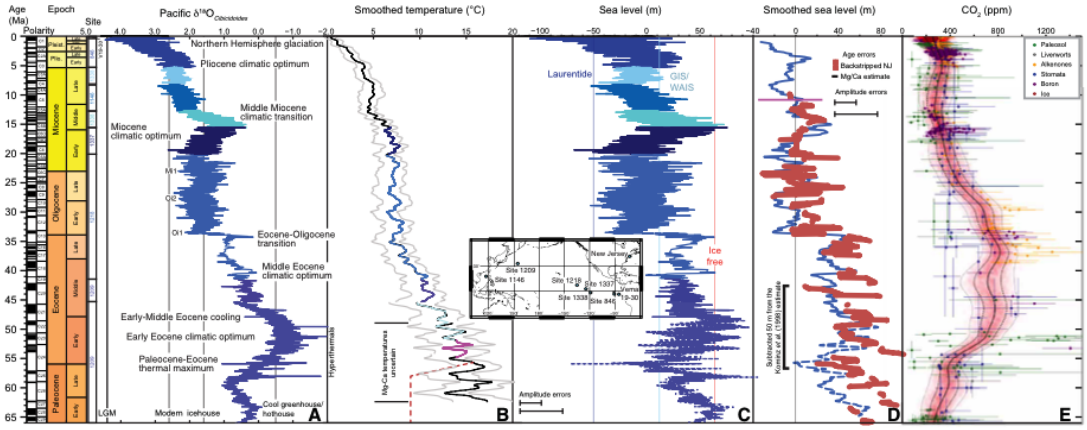

Figure 1. Summary of Cenozoic benthic foraminiferal $\delta^{18}O$, temperature, sea level, and CO_2 records.

8. 描述单畴颗粒热化学剩磁获得的动力学方程的精确解析解：对于绝对古强度确定的意义

翻译人：张伟杰 12031188@mail.sustech.edu.cn

Shcherbakov V, Lhuillier F, Sycheva N K. ***Exact analytical solutions for kinetic equations describing thermochemical remanence acquisition for single-domain grains: Implications for absolute paleointensity determinations*** *[J]. Journal of Geophysical Research: Solid Earth. 2021, 126(5): e2020JB021536.*

https://doi.org/10.1029/2020JB021536

摘要：火山岩的热剩磁(TRM)或者热化学剩磁（TCRM）是恢复地球历史时期绝对地磁场强度的关键，但是剩磁的获得强烈依赖于剩磁获得过程中的动力学条件。本文给出了单轴形状各向异性的非相互作用单畴颗粒与时间相关的热剩磁获得和热退磁过程的精确解析解。我们的解是在比以前研究更少限制条件下获得的，对于颗粒体积增大或通过提高居里点（T_c）获得 TCRMs 都是有效的。我们首先证明了通过 T_c 增加获得的 TCRM 与 TRM 具有相当的古强度结果，然而通过体积增大获得的 TCRM 具有明显更低的古强度结果。然后，我们模拟了多种矫顽力颗粒集合体的 Arai-Nagata 图，发现 TRM 及通过增大 T_c 获得的 TCRM 可以使用所有的 Thellier 类方法产生了可靠的绝对古强度解果。然而，通过体积增大获得的 TCRM 产生了弯曲的 Arai-Nagata 图。最明显的动力学效应是冷却速率对绝对古强度测定的影响，因为冷却时间增加到 10 倍，剩余磁化强度增加了约 5%。当自然样品的冷却时间与地磁场长期变化的时间尺度一致时，这种情况下得到的结果会出现问题。冷却时间足够长去平均掉长期变化的情形可以通过使用冷却速率矫正得到可靠的绝对古强度结果。

ABSTRACT: The magnetic record, preserved by igneous rocks in the form of thermoremanent magnetization (TRM) or thermo-chemical remanent magnetization (TCRM), is essential to reconstruct Earth's absolute paleointensity (API) but strongly depends on the kinetic conditions in which the remanence was acquired. In this paper, we present exact analytical solutions describing the time-dependent processes of

acquisition and thermal demagnetization of various kinds of thermally activated remanences for non-interacting single-domain grains with uniaxial shape anisotropy. Our solutions, derived in less-restrictive conditions than previous studies, are also valid for TCRMs acquired either by growth of grain volume or by increase of the Curie point T_c. We first show that TCRMs by T_c increase and TRMs are of comparable intensity whereas TCRMs by volume growth are significantly less intense. We then model Arai-Nagata diagrams for assemblies of coercivity-variable grains and find that all Thellier-type protocols yield reliable API determinations for TRMs and TCRMs by T_c increase, with the peculiarity of the IZZI protocol to produce small zigzags in the Arai-Nagata diagram. In contrast, TCRMs by volume growth yield convex Arai-Nagata diagrams. The most conspicuous kinetic effect is the influence of cooling rate on API determinations due to a ~5% increase of the remanent magnetization for a 10-fold increase in cooling time. We show that the situation is problematic when the cooling time of natural samples coincides with the geomagnetic secular-variation time scales. Natural samples with cooling times sufficient to average out secular variation conversely yield reliable API determinations provided a cooling rate correction is applied.

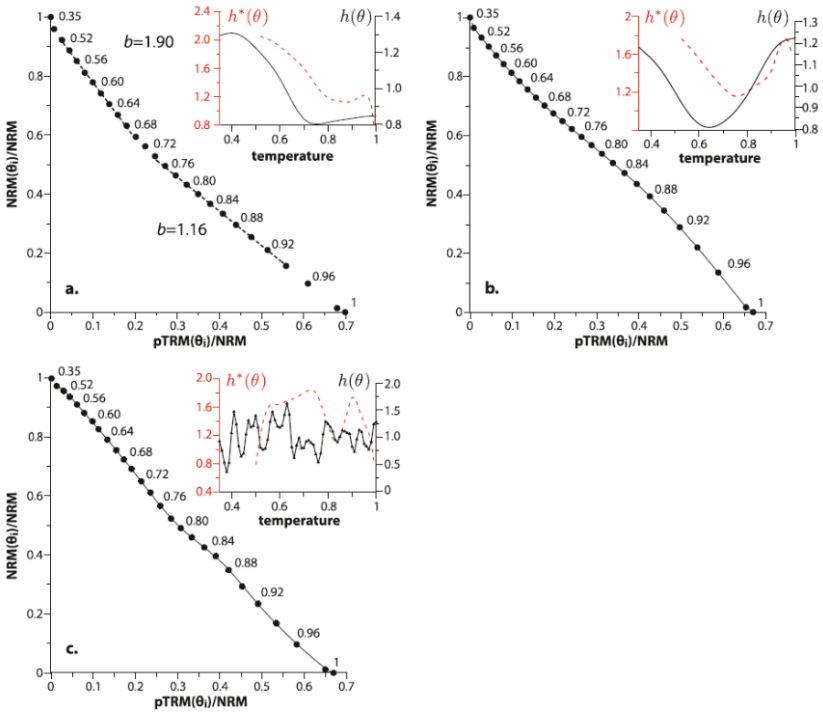

Figure 1. Effect of secular variation on Arai-Nagata diagrams for Thellier–Coe experiments. (a and b) TRM acquired for cooling time λ_{NRM} = 1,000 years (i.e., q = 42.6). (c) TRM acquired for cooling time λ_{NRM} = 10,000 years (i.e., q = 44.9). The variations of the normalized external field h($\theta = 1 - t / \lambda | \lambda \geq 0.5$) during the TRM acquisition (solid line, right axis in the insets) were predicted by the statistical model by Khokhlov and Shcherbakov (2015). The local value of the paleointensity in the Arai-Nagata diagrams is represented by the derivative h*(θ) = d(NRM)/d(pTRM) (dashed line, left axis in the insets).

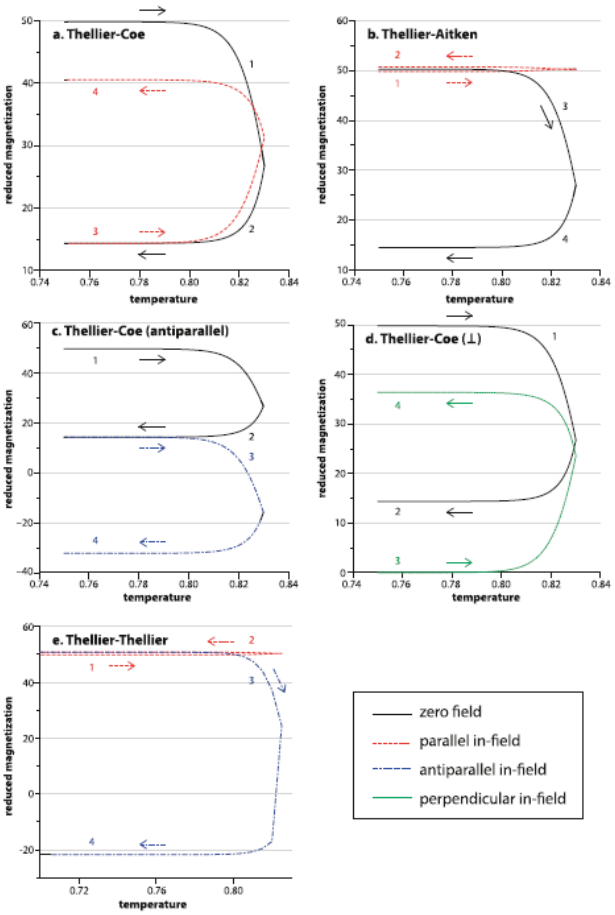

Figure 2. Continuous thermomagnetic curves of the reduced magnetization y(θ) to an intermediate temperature θi = 0.83 for an ensemble of identical SD grains with parameters g = 100 and q = 25. (a) Zero-field heating–cooling cycle (curves 1–2) followed by an in-field heating–cooling cycle (curves 3–4), following the example of the Thellier–Coe protocol. (b) In-field heating–cooling cycle (curves 1–2) followed by a zero-field heating–cooling (curves 3–4), following the example of the Thellier–Aitken protocol. (c) Same as panel (a) for a laboratory field antiparallel to the TRM direction. (d) Same as panel (a) for a laboratory field perpendicular to the TRM direction. (e) Example of the Classical Thellier method with opposite fields applied for the first and second cycles.

9. 全新世大暖期格陵兰岛的变暖及其影响

翻译人：李海 12031330@mail.sustech.edu.cn

Axford Y, de Vernal A, Osterberg E C. ***Past Warmth and Its Impacts During the Holocene Thermal Maximum in Greenland*** *[J]. Annual Review of Earth and Planetary Sciences, 2020, 49: 279-307. https://doi.org/10.1146/annurev-earth-081420-063858*

摘要：全新世早期至中期，较高的夏季日照导致整个北极地区数千年的夏季变暖。相较于地质历史时期的气候变暖，现代气候变暖原因明显不同，但是过去暖期的地质数据可为未来提供经验。作者利用格陵兰地区的冰芯、湖泊和海洋沉积物记录重建全新世的温度变化，其中夏季温度对冰盖质量平衡、海洋环流和海冰的影响，在全球范围内具有重要意义。发现全新世大暖期格陵兰岛的夏季温度比二十世纪中叶的夏季高 3-5℃，这比通常认为的更早、更强。气候变暖带来了巨大的后果：许多冰川消失、常年海冰消退、动植物的北移、格陵兰冰盖迅速萎缩、冰川融水增加导致海水强烈分层和部分地区冬季海冰增加。

ABSTRACT: Higher boreal summer insolation in the early to middle Holocene drove thousands of years of summer warming across the Arctic. Modern-day warming has distinctly different causes, but geologic data from this past warm period hold lessons for the future. We compile Holocene temperature reconstructions from ice, lake, and marine cores around Greenland, where summer temperatures are globally important due to their influence on ice sheet mass balance, ocean circulation, and sea ice. Highlighting and accounting for some key issues with proxy interpretation, we find that much of Greenland experienced summers 3 to 5°C warmer than the mid-twentieth century in the early Holocene--earlier and stronger warming than often presumed. Warmth had dramatic consequences: Many glaciers disappeared, perennial sea ice retreated, plants and animals migrated northward, the Greenland Ice Sheet shrank rapidly, and increased meltwater discharge led to strong marine water stratification and enhanced winter sea ice in some areas.

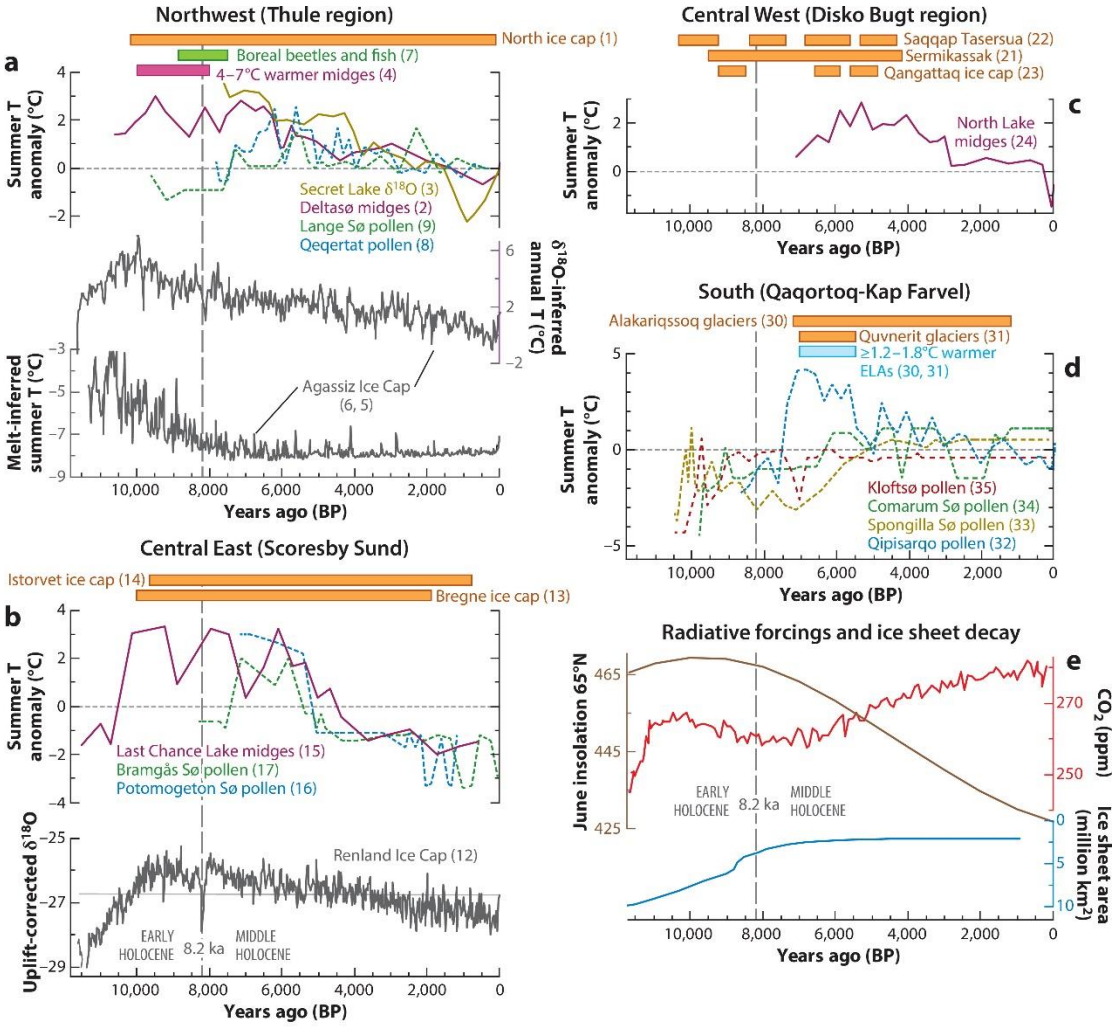

Axford Y, et al. 2021
Annu. Rev. Earth Planet. Sci. 49:279–307

Figure 1. (a–d) Holocene air temperature indicators. Colored bars show qualitative indicators of summers warmer than the mid-twentieth century AD (smaller-than-present mountain glaciers and ice caps in orange; northward migrations of terrestrial species in green) and discontinuous quantitative estimates (red) from midge assemblages and reconstructed glacier equilibrium line altitudes (ELAs) (light blue). Colored curves show summer temperature anomalies relative to the mid-twentieth century. Gray curves show data from large marginal ice caps. $\delta^{18}O$ from ice cores is an annual proxy. Note the divergence between pollen-based reconstructions (dashed data curves) and other indicators in the early Holocene, whereas all indicators largely agree through the middle and late Holocene. The numbers in parentheses refer to the code numbers in Figure 1b and Supplemental Table 1. (e) Climate forcings and influences including June insolation (Berger & Loutre 1991), atmospheric CO_2 (Monnin et al. 2004), and decline of the Laurentide-Innuitian-Cordilleran ice sheet complex (Dalton et al. 2020, y-axis reversed).

10. 欧洲四千年古地磁场模型 SCHA.DIF.4k 及其在定年中的应用

翻译人：柳加波 liujb@sustech.edu.cn

Pavón-Carrasco F J, Campuzano S A, Rivero-Montero M, et al. ***SCHA. DIF. 4k: 4,000 Years of Paleomagnetic Reconstruction for Europe and Its Application for Dating*** *[J]. Journal of Geophysical Research: Solid Earth, 2021, 126(3): e2020JB021237.*

https://doi.org/10.1029/2020JB021237

摘要：自 2009 年欧洲古地磁场模型 SCHA.DIF.3k 发布以来，来自欧洲的考古材料（例如烤制黏土）和火山岩的古地磁方向数据增加了约 90%，古强度数据增加了约 180%。基于欧洲古地磁数据的快速增长，我们更新了之前的区域古地磁模型，称之为 SCHA.DIF.4k。SCHA.DIF.4k 适用于欧洲大陆及其邻近地区，并跨越了过去四千年。为了对地磁场三要素（偏角、倾角和强度）进行建模，我们使用了区域 R-SCHA2D 方法进行时间和空间上的三次样条插值。我们对以 40° N 和 10° E 为中心，30° 圆形范围内的现有考古和火山岩古地磁数据进行了严格筛选。为了更好地限制最近几百年的古磁场变化，我们也加入了 HISTMAG 汇编的历史古地磁记录。新的 SCHA.DIF.4k 使我们能够更好地定义整个欧洲的古磁场，并为古地磁定年提供新的地磁场长期变化曲线。我们评估了使用这些曲线进行定年的精度。结果表明，定年精度很大程度上仍取决于目标古地磁数据的可靠性、时间上的分辨率以及古地磁场自身的变化。此外，使用完整的矢量地磁场记录（包含方向和强度），而不是仅仅基于方向，能够获得更精确的古地磁年代。

ABSTRACT: Since the publication of the European archaeomagnetic field model SCHA.DIF.3k in 2009, the number of paleomagnetic data derived from archaeological materials such as baked clays and volcanic rocks coming from Europe has increased by about 90% for directions and around 180% for intensities. Taking advantage of this increase, here we provide an updated regional archaeomagnetic model, called SCHA.DIF.4k, for the European continent and adjacent areas and now covering the last four millennia. To model the three geomagnetic elements, declination, inclination, and

intensity, we use the regional R-SCHA2D technique in space and temporal basis of cubic splines. A critical selection of the archaeomagnetic and volcanic data available in a spherical cap of 30° centered at 40°N latitude and 10°E longitude has been considered. In addition, in order to better constrain the behavior of the archaeomagnetic field during the last centuries, we include the historical data of the HISTMAG compilation. The new regional model allows us to better define the paleomagnetic field over Europe as well as to generate new paleosecular variation curves for archaeomagnetic dating purposes. Using these curves, the dating precision has been estimated for the last 4 kyr. As expected, results show that it strongly depends on the data uncertainties, the temporal data distribution and the behavior of the geomagnetic field itself. In addition, the use of the full vector geomagnetic field, instead of the directional information exclusively, provides more precise archaeomagnetic dating results.

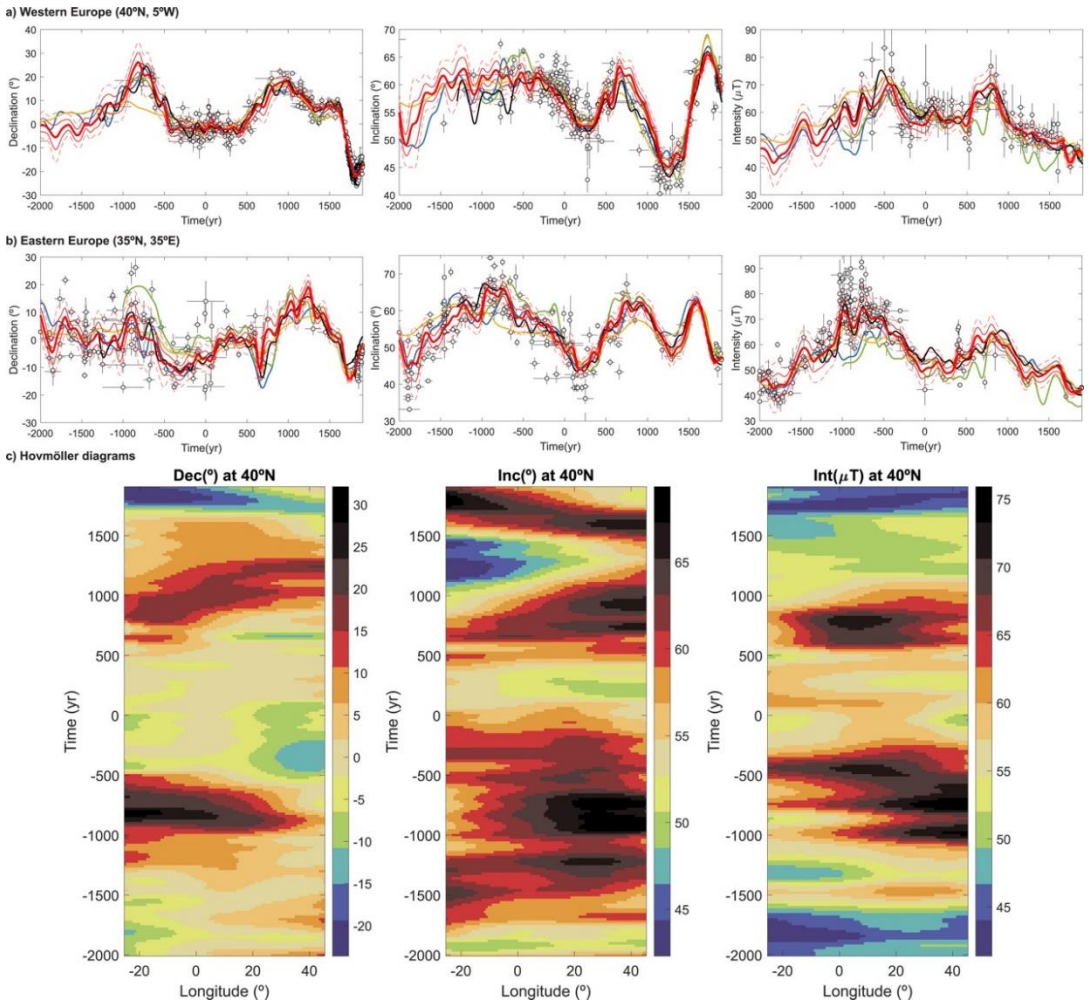

Figure 1. Paleosecular variation (PSV) curves at (a) 40°N, 5°W and (b) 35°N, 35°E coordinates, and (c) Hovmöller diagrams for the declination (left), inclination (center), and intensity (right) elements. For the PSV curves: red curves correspond to the new SCHA.DIF.4k model with error bands at 1σ (thin red lines) and 2σ (dashed red lines). Green curves represent the previous regional archaeomagnetic model SCHA.DIF.3k. In addition, global archaeomagnetic models CALS10k.2 (yellow curves), SHA.DIF.14k (blue curves) and SHAWQ family (black curves) are also plotted. Archaeomagnetic and historical data referred to each location are plotted for comparison as gray dots (with error bars). For the Hovmöller diagrams: they are calculated at a constant latitude of 40°N for the range of longitudes inside the spherical cap.

11. 南美陆地上二叠纪末大灭绝延后的证据

翻译人：蒋晓东 jiangxd@sustech.edu.cn

Viglietti P A, Benson R B J, Smith R M H, et al. ***Evidence from South Africa for a protracted end-Permian extinction on land*** *[J]. PNAS, 2021, 118: 17.*

https://doi.org/10.1073/pnas.2017045118

摘要：地球上最大的生物灭绝事件出现在二叠-三叠转换期（PTT）。陆地上的这次事件见证了恐龙合弓纲到首龙次纲为主动物群落的转变以及陆地生态系统的转变。然而，由于缺少高精度的化石数据来确定该事件亚百万年尺度的变化，因此对于灭绝模式的理解仍然受到限制。我们分析了来自南美卡鲁盆地的 588 个四足动物化石，沉积年代横跨 4 百万年，平均 30 万年的 13 个地层区段。通过使用样本标准化方法，我们描述了 PTT 动物群落的动力学。发现在延后 1 百万年的区段区域性灭绝率较高，而最初与低发生率同时发生。这引起群落多样性衰退到了灭绝的临界值，接近于二齿兽（Daptocephalus）组合到水龙兽（Lystrosaurus）组合在的转换边界。在该边界之上区域起源速率突然增加，同时伴随着高灭绝速率，这驱动了群落快速翻转和生态系统不稳定的短寿命物种群落。灾难分类群水龙兽表现出从早二叠纪开始并且长时间尺度的丰度增加趋势。大规模灭绝开始时，水龙兽占群体 54%，灭绝后占群体的 70%。早期水龙兽丰度变化表明环境变化引起了水龙兽扩展，而不是通常假设的其他物种灭绝后的生态机会。我们的发现保守地认为卡鲁灭绝的时间间隔非常近，但与更迅速的海洋事件并不一致，并且揭示了陆地和海洋 PTT 灭绝之间的关键差异。

ABSTRACT: Earth’s largest biotic crisis occurred during the Permo–Triassic Transition (PTT). On land, this event witnessed a turnover from synapsid- to archosauromorph-dominated assemblages and a restructuring of terrestrial ecosystems. However, understanding extinction patterns has been limited by a lack of high-precision fossil occurrence data to resolve events on submillion-year timescales. We analyzed a unique database of 588 fossil tetrapod specimens from South Africa’s Karoo Basin,

spanning ~4 My, and 13 stratigraphic bin intervals averaging 300,000 y each. Using samplestandardized methods, we characterized faunal assemblage dynamics during the PTT. High regional extinction rates occurred through a protracted interval of ~1 Ma, initially co-occurring with low origination rates. This resulted in declining diversity up to the acme of extinction near the Daptocephalus–Lystrosaurus declivis Assemblage Zone boundary. Regional origination rates increased abruptly above this boundary, co-occurring with high extinction rates to drive rapid turnover and an assemblage of short-lived species symptomatic of ecosystem instability. The "disaster taxon" Lystrosaurus shows a long-term trend of increasing abundance initiated in the latest Permian. Lystrosaurus comprised 54% of all specimens by the onset of mass extinction and 70% in the extinction aftermath. This early Lystrosaurus abundance suggests its expansion was facilitated by environmental changes rather than by ecological opportunity following the extinctions of other species as commonly assumed for disaster taxa. Our findings conservatively place the Karoo extinction interval closer in time, but not coeval with, the more rapid marine event and reveal key differences between the PTT extinctions on land and in the oceans.

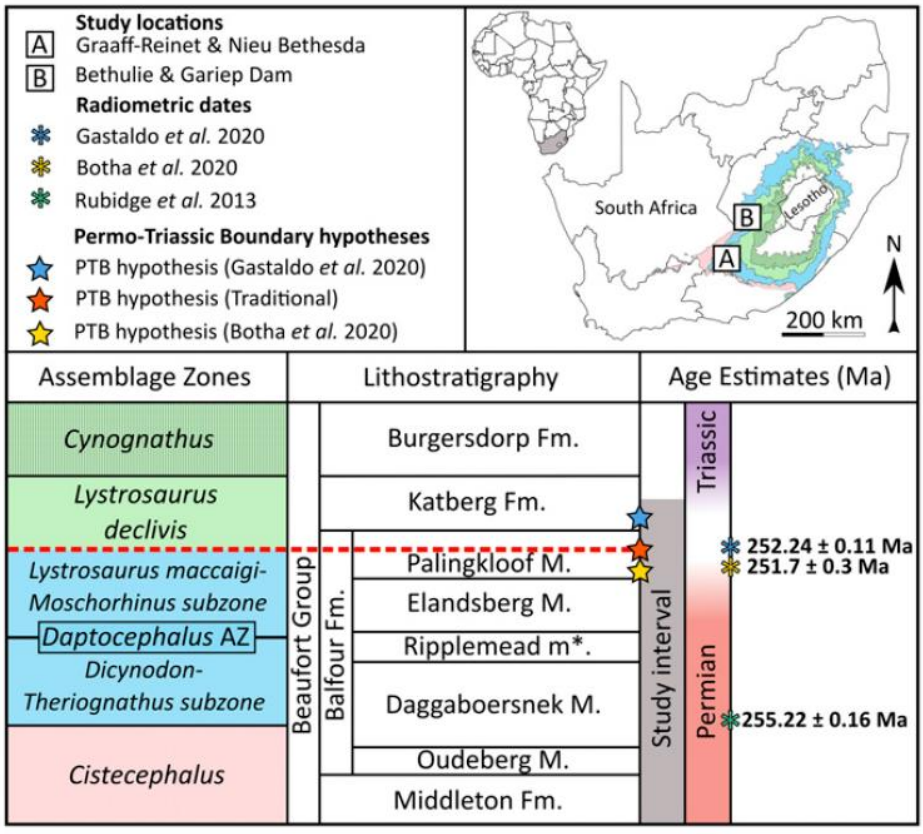

Figure 1. Map of South Africa depicting the distribution of the four tetrapod fossil assemblage zones (Cistecephalus, Daptocephalus, Lystrosaurus declivis, Cynognathus) and our two study sites where fossils were collected in this study (sites A and B). Regional lithostratigraphy and biostratigraphy within the study interval are shown alongside isotope dilution–thermal ionization mass spectrometry dates retrieved by Rubidge et al., Botha et al., and Gastaldo et al. The traditional (dashed red line) and associated PTB hypotheses for the Karoo Basin are also shown. Although traditionally associated with the PTB, the Daptocephalus–Lystrosaurus declivis Assemblage Zone boundary is defined by first appearances of co-occurring tetrapod assemblages, so its position relative to the three PTB hypotheses is unchanged. The Ripplemead member (*) has yet to be formalized by the South African Committee for Stratigraphy.

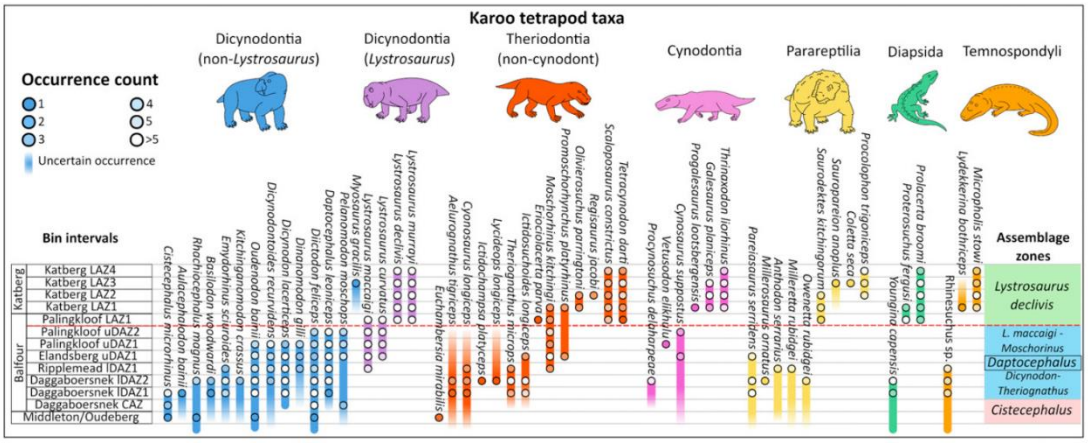

Figure 2. Stratigraphic ranges of the 53 Karoo fossil tetrapod species included in this study with occurrence counts (infilled circles) in each bin interval. The dashed red line indicates the Daptocephalus–Lystrosaurus declivis Assemblage Zone boundary, the traditional PTB in the Karoo Basin. Some species have lower-resolution stratigraphic data, and these were included here (but not in the analyses) to show uncertain first or last occurrences for specific species in our study.

12. 云南剑川盆地古金沙江古近系沉积记录

翻译人：刘伟 inewway@163.com

He M, Zheng H, Clift P, et al. ***Paleogene sedimentary records of the paleo-Jinshajiang (Upper Yangtze) in the Jianchuan Basin, Yunnan, SW China*** *[J]. Geochemistry, Geophysics, Geosystems, 2021. online*

https://doi.org/10.1029/2020GC009500

摘要：新生代青藏高原地表隆起造成了亚洲大型水系的诞生和重组。长江的发育与高原隆升密切相关，对区域构造地貌过程具有重要意义，但目前仍存在争议。关键的科学问题是长江上游(金沙江上游)是否曾向东南流向南海。本文对建川盆地古近系宝相寺组、金丝厂组和双河组沉积岩进行物源分析。我们将其与其他区域性盆地的类似沉积物进行了比较，并与潜在的来源进行了比较。重矿物和地球化学资料表明，金丝厂组沉积物较双河组和宝相寺组更为成熟。金丝厂组为大型河流体系的产物，宝相寺组则以局部物源为主。双河组的物质既有来自远方的物质，也有来自局部侵蚀的物质。剑川盆地碎屑锆石 U-Pb 年龄与贡觉盆地、思茅盆地和楚雄盆地沉积物中锆石 U-Pb 年龄相似，与现代金沙江具有较大的相似性。锆石年龄统计分析表明，松潘-甘孜地块是所有沉积物的主要来源，扬子克拉通和北羌塘地块则是次级来源。综合这些资料，证实古金沙江在始新世晚期由青藏高原东南部向南流向南海，制约了长江第一弯的形成时代。

ABSTRACT: Cenozoic surface uplift of Tibetan Plateau has driven the birth and reorganization of large river systems in Asia. The development of the Yangtze River, closely linked to plateau uplift, has important implications for the regional tectonic-geomorphology processes, but is still under debate. The key scientific question is whether the upper Yangtze (upper Jinshajiang) once flowed southeast to the South China Sea. In this study, we carried out provenance analysis on Paleogene sedimentary rocks in the Jianchuan Basin, composed of the Baoxiangsi, Jinsichang and Shuanghe formations. We compared them with similar deposits in other regional basins, as well

as with potential sources. Heavy-mineral and geochemical data show that sediments from the Jinsichang Formation are more mature compared with those from the Shuanghe and Baoxiangsi formations. The Jinsichang Formation represents the products of a large fluvial system, whereas the Baoxiangsi Formation is mainly dominated by local sources. The Shuanghe Formation contains material from both distant sources and locally eroded materials. Detrital zircon U-Pb age patterns from the Jianchuan Basin are similar to those in sediments in the Gonjo, Simao and Chuxiong basins, and show great similarity with the modern Jinshajiang River. Statistical analysis of the zircon ages suggests that the Songpan-Ganzi terrane was the primary source for all sediments, while the Yangtze Craton and northern Qiangtang terrane constitute secondary sources. Taken together these data confirm that a paleo-Jinshajiang flowed south towards to the South China Sea from the SE Tibetan Plateau in the late Eocene, constraining the age of formation of the First Bend.

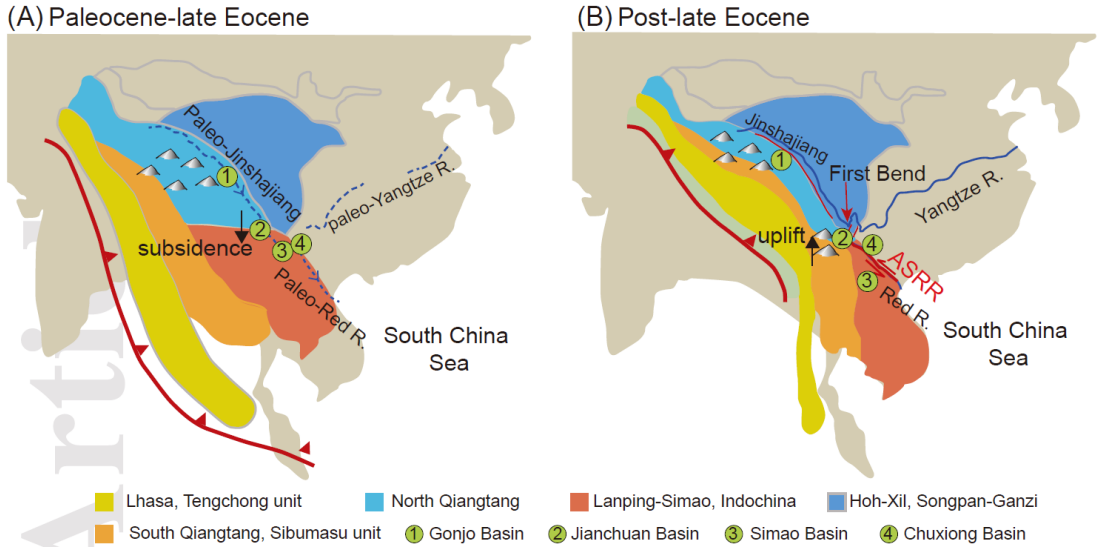

Figure 1. Schematic evolutionary model of the paleo-Jinshajiang, illustrating the formation of the First Bend. (A) the paleo-Jinshajiang draining from the Tibetan Plateau southward to the South China Sea, flowing through the Gonjo, the Jianchuan and the Simao Basin during Paleocene- late Eocene. (B) After the late Eocene, the drainage changed to northeast and formed the First Bend because of the uplift and inversion of the Jianchuan Basin and the left-sinistral motion of the ASRR. The positions of the terranes and its reconstrucitions are based on Royden et al. (2008).

13. 印度夏季风降水氧同位素年际变化反映了水汽来源的变化

翻译人：杨会会 11849590@mail.sustech.edu.cn

Kathayat G, Sinha A, Tanoue M, et al. ***Interannual oxygen isotope variability in Indian summer monsoon precipitation reflects changes in moisture sources*** *[J]. Communications Earth & Environment, 2021, 2: 96.*

https://doi.org/10.1038/s43247-021-00165-z

摘要：印度夏季风域降水氧同位素组成时空变化的主要影响因素受到有限观测记录的限制。因此，该地区指标档案中保存的降水同位素特征的气候意义仍不清楚。本文我们提出了一种具有水分标记能力的同位素气候模型(IsoGSM2)，以研究来自海洋和陆地的水分对夏季季风降水氧同位素组成年际变化的相对贡献的作用。在弱季风年，阿拉伯海对印度次大陆降水的贡献占主导地位，而在强季风年，遥远的海洋和陆地源对印度次大陆降水的影响较大。结果表明，该地区季风环流、水汽来源和降水强度的变化是相互关联的，其石笋氧同位素记录有助于重建年际至年代际季风降水变化。

ABSTRACT: The primary influences on the spatio-temporal variability of oxygen isotope compositions in precipitation over the Indian summer monsoon domain are inadequately constrained by the limited observational record. Consequently, the climatic significance of isotopic signatures of precipitation preserved in proxy archives from the region remains unclear. Here we present simulations with an isotope-enabled climate model (IsoGSM2) with the moisture-tagging capability to investigate the role of relative contributions of moisture from oceanic and terrestrial sources to the interannual variability in oxygen isotope composition in summer monsoon rainfall. During weak monsoon years, the moisture contribution from the Arabian Sea dominates precipitation over the Indian subcontinent while the remote oceanic and terrestrial sources have a greater influence during strong monsoon years. We suggest that changes in monsoon circulation, moisture source, and precipitation intensity are interrelated and

that speleothem oxygen isotope records from the region can potentially help reconstruct interannual to decadal monsoon rainfall variability.

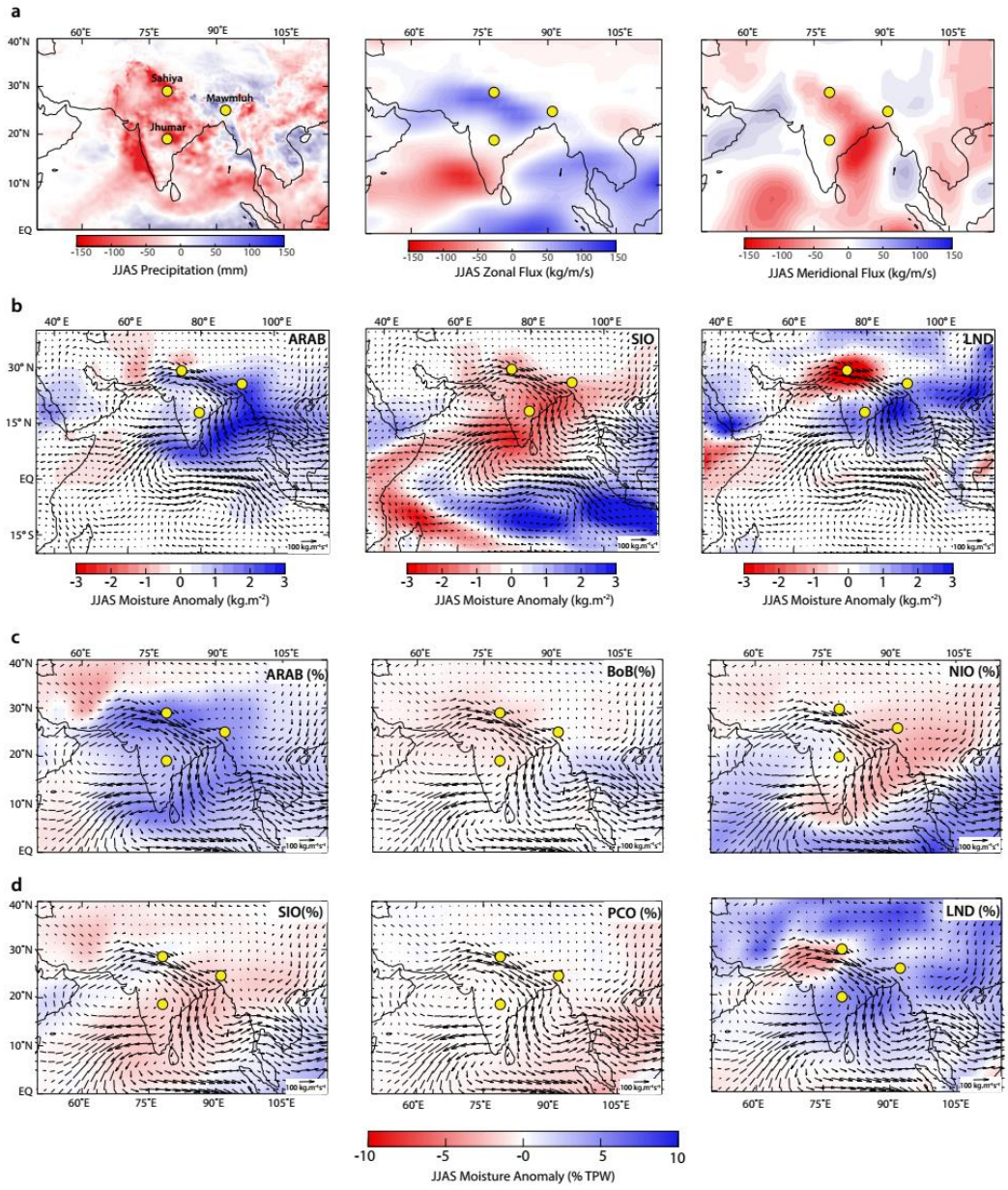

Figure 1. Weak minus strong JJAS composites of climatological fields and "tagged" moisture anomalies. a JJAS mean precipitation anomalies from the European Centre Medium-Range Weather Forecasts Reanalysis Fifth generation (ERA-5)71 (left), vertically integrated zonal flux anomalies (middle), and meridional moisture flux anomalies (right) from ERA-571 (shaded). b JJAS moisture anomalies from ARAB (left), SIO (middle), and LND (left). c, d JJAS moisture (% TPW) (shaded) from ARAB (left), BoB (middle), NIO (right), SIO (left), PCO (middle), LND regions (right) are superimposed by simulated vertically integrated moisture flux anomalies over the same period

(1979–2010). Circles in all panels mark the locations of the cave records discussed in the text. The strong (1983, 1988, and 1994) and weak (1982, 1987, 2002, 2004, and 2009) monsoon seasons are defined as positive (negative) departures of one standard deviation from the mean of All India Rainfall. The weak monsoon years are characterized by (i) negative precipitation anomalies over much of continental India except over northeast, northern BoB, and the coastal Myanmar regions; (ii) reduced vertically integrated zonal moisture flux along the climatological axis of the LLJ over the Arabian Sea, compensated by anomalously enhanced northwest-southeast trending zonal moisture flux across north India (with its core at ~25°N) and near the equator; (iii) negative meridional moisture flux anomalies, particularly east of 75°E over the Indian subcontinent.

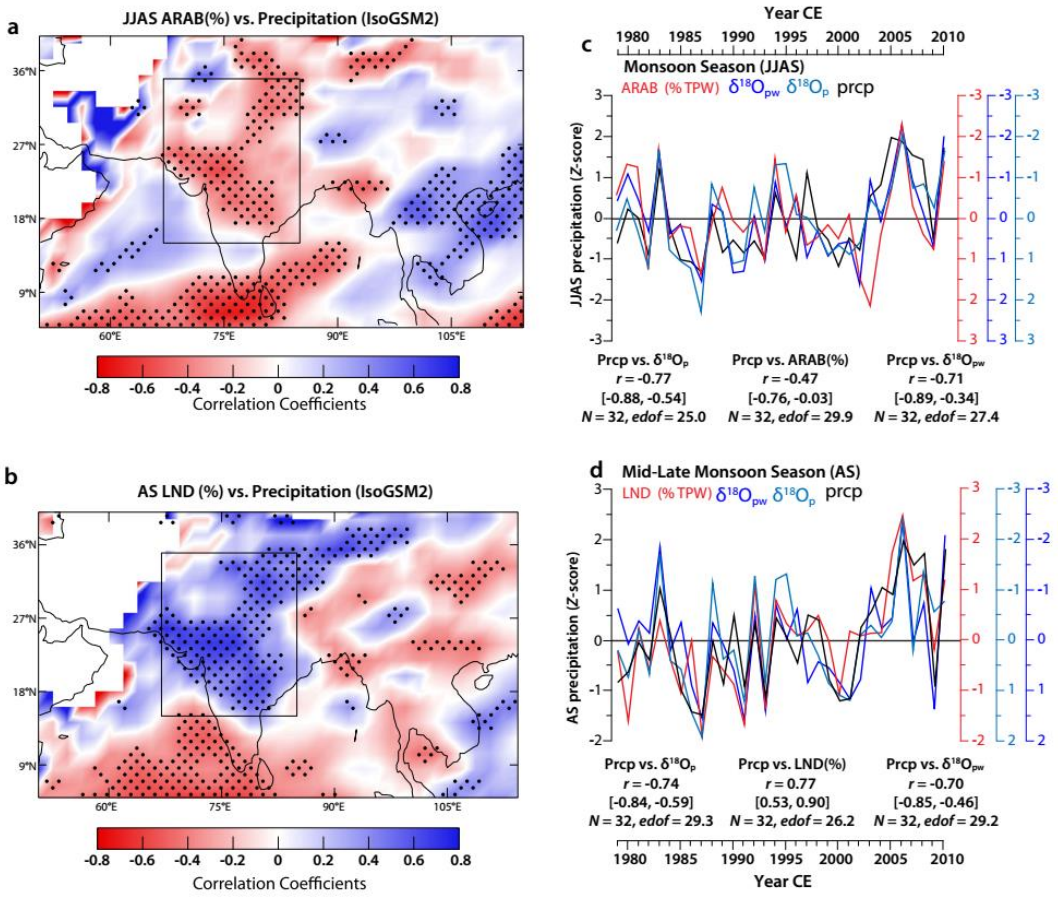

Figure 2. Spatial correlation fields and time-series comparisons. a Correlations between June and September (JJAS) IsoGSM2 simulated ARAB (% TPW) and precipitation amount at each grid cell. The correlation was performed after removing the climatological mean and trend from data (b) same as (a) but for LND (% TPW) vs. August to September (AS) precipitation amount. The black

rectangle in each panel marks the region used for extracting time-series comparisons in panels (c) and (d). Stippling indicates regions of significant correlations at 95% significance level obtained after accounting for serial correlations and followed by the application of false discovery rate (FDR) procedure with a 5% threshold (see "Methods"). FDR is the expected proportion of rejected hypotheses when the null hypothesis is actually true for those tests. c Z-score transformed time-series comparisons between the JJAS precipitation amount (black), ARAB (% TPW) (red), $\delta^{18}O_p$ (cyan), and $\delta^{18}O_{pw}$ (blue) for 1979–2010. Timeseries for all four variables represent averaged values extracted from a rectangular-shaped region over the Indian subcontinent marked by rectangles in panels (a) and (b). All vertical axes (right) are reversed and color-coded by variables names. d Same as c but for August to September precipitation and LND (%) moisture source. The vertical axes for $\delta^{18}O_p$ and $\delta^{18}O_{pw}$ are reversed. The Pearson correlation coefficients (r) with 95% confidence intervals (CI) are shown in each panel. The 95% CI is derived from pairwise moving-block bootstrap resampling (N = 2000) and calibration that account for serial autocorrelation in data (see "Methods").